Novel Techniques in Quantum Optics

Confocal Super-Resolution Microscopy Based on a Spatial Mode Sorter and Herriott Cell as an Image-Preserving Delay Line

Katherine Karla Misaye Bearne

Thesis submitted to the University of Ottawa
in partial fulfillment of the requirements for the
Master of Science degree in Physics
under the supervision of Robert W. Boyd

Department of Physics
University of Ottawa
Canada

Abstract

Breaking Rayleigh's "curse" and resolving infinitely small spatial separations is one motivation for developing super-resolution in imaging systems. It has been shown that an arbitrarily small distance between two incoherent point sources can be resolved through the use of a spatial mode sorter, by treating it as a parameter estimation problem. However, when extending this method to general objects with many point sources, the added complexity of multi-parameter estimation problems makes resolution of general objects quite challenging. In the first part of this thesis, we propose a new approach to deal with this problem by generalizing the Richardson-Lucy (RL) deconvolution algorithm to accept the outputs from a mode sorter. We simulate the application of this algorithm to an incoherent confocal microscope using a Zernike spatial mode sorter rather than the conventional pinhole. Our method can resolve general scenes with arbitrary geometry. For such spatially incoherent objects, we find that the resolution enhancement of the sorter-based microscopy using the generalized RL algorithm is over 30% higher than the conventional confocal approach using the standard RL algorithm. This method is quite simple and potentially can be used for various applications including fluorescence microscopy. It could also be combined with other super-resolution techniques for enhanced results. The second part of this thesis explores the potential for the Herriott cell to be used as an image-preserving delay line. In quantum imaging, entangled photons are often utilized to take advantage of their spatial and temporal correlations. One photon ("the signal") interacts with the system to be measured and the other ("the herald") is used to trigger the detection of the signal. However, for a typical high-sensitivity camera, there is a delay on the order of 20 ns between the trigger and the sensor becoming active allowing for the signal to be recorded. An image-preserving delay line (IPDL) serves to store a photon without distorting the spatial structure and losing the spatial and temporal correlations. It is commonly made with a series of 4f systems to repeatedly image the light field. We propose to use the Herriott cell as an image-preserving delay line. We tested 10 of the lower-order HG modes and found it was able to preserve almost all of them with high fidelities (>90%), with the only exceptions being the largest modes (HG03 and HG30) at the longest delay (7.9 m) where the fidelity was still >86%. In addition to these modes, it was also able to store general images. This application of the Herriott cell affords insights into miniaturizing IPDLs, which tend to occupy a significant amount of space. Overall, these two projects offer novel insight and application to the world of quantum imaging.

Statement of Originality and Collaborative Contributions

To the best of her knowledge, the author states that the projects and work described in this Master's thesis constitute original research in the field of physics. Here we describe the contributions from different individuals on the various aspects of each project.

This thesis was supervised in its entirety by Dr. Robert W. Boyd and both projects fall under

his guidance. Additionally, Dr. Boris Braverman was the postdoctoral fellow responsible for direct oversight of Katherine Bearne and assisting with these projects.

For the work on the Richardson-Lucy sorter-based deconvolution algorithm described in Chapter 2, Dr. Yiyu Zhou initiated the project, having the original idea and creating the code. K. Bearne worked on the development of the method, data collection, and analysis with help and supervision from Dr. Zhou and Dr. Braverman. K. Bearne along with all included co-authors Yiyu Zhou, Boris Braverman, Jing Yang, S. A. Wadood, Andrew N. Jordan, A. N. Vamivakas, Zhimin Shi, and Robert W. Boyd contributed to writing the manuscript. More detail may be found in Chapter 2.

For the work on the Herriott cell described in Chapter 3, Dr. Braverman conceived the original idea and provided both oversight and assistance throughout the project. K. Bearne performed the simulations, devised experimental design and setup, and collected and analyzed the data.

Acknowledgements

I will forever be grateful to Dr. Robert W. Boyd for my initial introduction into the world of optics research. Beginning with my first co-op as an undergraduate, Dr. Boyd has always encouraged me to pursue the questions that interest me and let that guide my research. He has led an incredible group of people and I would like to thank the Boyd group as a whole for creating a great lab and work environment. Thank you to Dr. Jeremy Upham for keeping me on track and organized with all the moving parts of my experiments.

I also thank the Canada Research Chairs (CRC) program and the Natural Sciences and Engineering Research Council of Canada (NSERC) for financial support.

Thank you to Dr. Boris Braverman for his endless patience in answering all of my questions and guiding me throughout my projects. I would never have been able to do these experiments without him teaching me little tricks and always making my life easier.

Another person who greatly contributed to both my projects and overall learning is Dr. Yiyu Zhou. Thank you for teaching me to recognize when you have publishable work and then how to write the paper. I appreciate his effort in teaching me super-resolution simulations as well as offering experimental advice even for projects he was not directly involved in.

Finally, I would like to thank my friends and family for motivating me and supporting me throughout my studies.

Contents

List of Figures

1 Overview

This thesis describes research on two separate projects. In the first project (Chapter 2), confocal microscopy with a spatial mode sorter is used to achieve super-resolution. This chapter is based on a published peer-reviewed paper which will be presented in full in Section 2.5. This thesis is intended to be a self-contained document. In order to provide sufficient background for the reader, an introduction to super-resolution is given in Section 2.2. More detail is also provided on the methods used in the paper in Section 2.3 for those who might be curious about the intricate details.

In the second project (Chapter 3), the potential for the Herriott cell to be used as an image-preserving delay line is explored. This project follows a more traditional approach to its content. As with the first project, a review of previous work is included in Section 3.1 in order to develop the motivation for using the Herriott cell as an image-preserving delay line. Following this, the simulation results are presented in Section 3.4, the experimental characterization is described in Section 3.6, and finally future projects are shown in Section 3.7

While these two projects may appear to be quite different on the surface, they both offer novel insights and applications to the world of quantum imaging, which will be illustrated in this thesis.

2 Super-resolution

This chapter is based on the following paper:

Bearne, K. K. M., Zhou, Y., Braverman, B., Yang, J., Wadood, S. A., Jordan, A. N., Vamivakas, A. N., Shi, Z., and Boyd, R. W. (2021). Confocal super-resolution microscopy based on a spatial mode sorter. Optics Express, 29(8), 11784-11792. https://doi.org/10.1364/oe.419493

2.1 Authorship

Since this manuscript has multiple authors, including a shared first author, I wish to clarify which tasks I performed and acknowledge the contributions of others. Dr. Yiyu Zhou originally conceived the idea of combining the spatial mode sorter with the Richardson-Lucy deconvolution algorithm to achieve super-resolution. He wrote the original MatLab code to perform the numerical simulations. In Section 2.3 the methods used and choices we made in developing this technique are elaborated upon. My role was to modify the code, test various images, and develop the appropriate parameter weights and stopping

criteria. I tested the experimental options and consultations with Dr. Boris Braverman and Dr. Zhou led to the sorter-based super-resolution approach outlined in the paper and Section 2.3. The manuscript was written by me, Dr. Zhou, and Dr. Braverman with contributions from all other co-authors.

2.2 Introduction to Super-resolution

2.2.1 Rayleigh Criterion

The primary purpose of an imaging system is to obtain the highest quality image possible to gather the most information about the object of interest. As such, enhancing spatial resolution is a common goal, with the field of super-resolution microscopy dedicated to techniques that allow for imaging with better resolution than the diffraction limit of light. This diffraction limit, known as Rayleigh's criterion [1] is the minimum separation distance required between two point sources in order for them to be resolved. An example of this is shown in **Figure 1**. Another example would be the Abbe criterion [2].

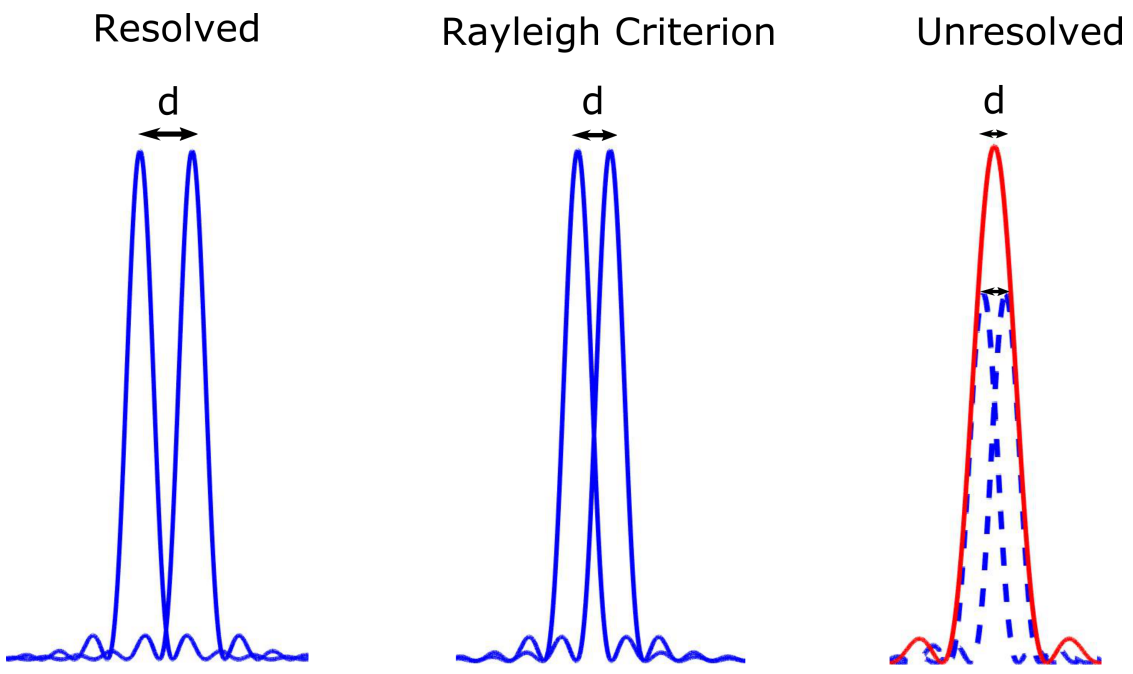

Figure 1: The separation distance (d) between two point sources determines whether they can be resolved or not. The minimum resolvable separation is given by the Rayleigh criterion.

The diffraction limit given by these two criteria $A_{Rayleigh} \approx 1.21$ and $A_{Abbe} = 1$ is explained by **Equation 1**, where d is the resolvable distance between features, A is a constant, λ is the wavelength of light, and NA is the numerical aperture of the imaging system. Note that this is the far-field diffraction limit.

$$d = A * \frac{\lambda}{NA}. \tag{1}$$

Examination of **Equation 1** considering the diffraction limit, reveals that there are multiple ways to decrease d. One could decrease λ, e.g., by imaging with UV or x-rays. Alternatively, one could increase NA, e.g., by using confocal, 4π, or structured illumination microscopy. Finally, one could avoid the far-field diffraction limit by imaging in the near-field, using near-field scanning optical microscopy (NSOM). Building on these ideas many different approaches have been developed, leading to various super-resolution techniques. To provide context for the present work relative to the other techniques used today, we present a brief overview of the more common super-resolution methods including their advantages and disadvantages.

2.2.2 General Resolution Increasing Techniques

Conventional confocal microscopy shown in Figure 1a in our work [3] (presented in full in Section 2.5) and reprinted here as **Figure 2** for convenience, uses a pinhole to spatially filter the light and generate a focused illumination spot. This illumination spot is scanned across the sample (x_1, y_1 in the object plane) to construct the full image [4].

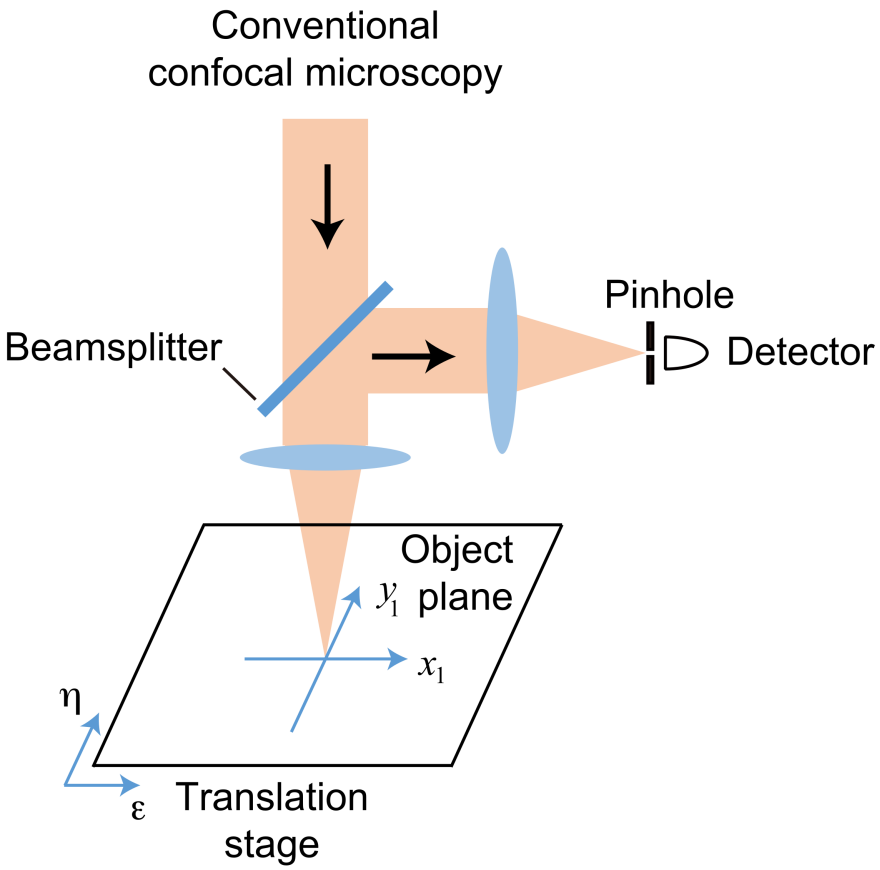

Figure 2: Figure 1a from Section 2.5 depicting the conventional confocal microscopy setup

Another scanning technique that focuses the light similar to a confocal microscope is 4π microscopy however, the light illuminating the sample is incident from both sides [5]. As shown in **Figure 3**, the 4π microscope consists of two opposing objective lenses. The input laser is split by a beam splitter and incident on the sample through both objectives (L1 and L2). The light emitted by the sample in response is then collected by these objectives and recombined at the beam splitter (BS). The dichroic (DC) mirror is used to reflect the illumination beam and transmit the emitted light to the detector.

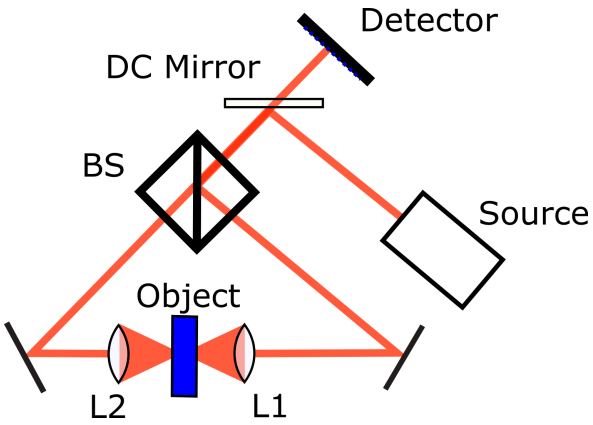

Figure 3: The setup for 4π microscopy with two opposing objective lenses (L1 and L2) to focus light onto the object is shown. The light is incident from both sides of the sample. The emitted light is recombined at the beam splitter (BS) where it passes through the dichroic (DC) mirror to the detector.

In structured illumination microscopy [6], the beam that illuminates the sample is structured or patterned, usually with stripes. The emitted fluorescence from the samples is then recorded. This process is repeated for various light structures. Interaction between the illumination beam pattern and the sample produces Moiré fringes which contain information about the sample. The information is computationally separated in Fourier space and properly repositioned before recombination to produce the final image.

Imaging systems are not perfect. Diffraction and aberrations or defects in the optics cause a single point to be seen as a blur, spread out in the image plane. This is characterized by the point spread function (PSF). The PSF is defined by the transverse spatial variation of the image compared to a point source object [7]. While the complex field distribution for a point source is given by the amplitude PSF, generally more emphasis has been placed on the intensity PSF which is simply the modulus squared of the amplitude [8]. Subsequent mentions of the PSF are therefore referring to the intensity PSF. In the case of the conventional confocal microscope, the PSF of the illumination beam is an Airy disk ($G(x_1, y_1)$) [9] described by **Equation 2** where (x_1, y_1) are the Cartesian coordinates and (r_1, θ_1) are the corresponding polar coordinates in the object plane, NA is the numerical aperture, λ is wavelength, and $k = 2\pi/\lambda$ is the wave number. J_1 is the first order Bessel function of the first kind [10]. For more details on the PSFs of the conventional and sorter-based confocal microscopy, please refer to the supplemental information of the manuscript found in Section 2.5.

$$G(x_1, y_1) = N_0 \left| J_1(k\mathrm{NA}r_1)/(\sqrt{\pi}r_1) \right|^2 . \tag{2}$$

The image produced by an imaging system is the convolution between the PSF of said imaging system and the object itself. Mathematically, the convolution is an integral transform. Put simply, the convo-

lution expresses how the shape of one function (our object) is modified by another (the PSF) giving the final image. In similar terms, deconvolution of images attempts to undo this blurriness caused by the PSF and return an image of the original object.

These imaging techniques offer modest improvements to the resolution and are commonly employed with additional methods to maximize the enhancement and achieve super-resolution.

2.2.3 Nonlinear Super-Resolution Techniques

Examples of nonlinear techniques include stimulated-emission depletion (STED) [11], photoactivated localization microscopy (PALM) [12], and stochastic optical reconstruction microscopy (STORM) [13]. While these methods allow us to overcome the diffraction limit, they typically require the use of specially prepared fluorescent samples, and the data collection can take extended periods of time. These limitations make the use of these methods impractical for many applications.

The principle behind STED is the inhibition of fluorescence in the outer regions of the excitation. A torus shaped beam is used to deplete specific regions of fluorophores through stimulated emission on a sample being imaged from the excited state. Consequently, the emitted light arises only from the more focused spot (at the centre of the torus) leading to higher resolution after raster scanning the STED beams over the whole sample. This is similar to the use of a pinhole to block the out-of-focus light in confocal microscopy, except in this case we attempt to avoid excitation of these external edges in the first place.

Another variation of this fluorescence microscopy technique is STORM. In this technique, the fluorescent molecules are "switched" on and off using different colored lights. Each molecule is adequately spaced from the others so that for each cycle all molecules can be resolved. Repeating this process allows for the determination of the positions of each fluorophore followed by reconstruction of the overall image.

Finally, PALM uses an activation protocol similar to the other techniques. Photoactivatable fluorescent proteins are attached to areas of interest, activated with a brief laser pulse, and then imaged. This process is repeated until all the fluorescent proteins have been activated and the supply of unbleached proteins is depleted. However, using the knowledge of the PSF for the imaging system, the location can be determined by fitting the expected image to the actual image. This allows for a better quality image whose resolution is dictated by the uncertainties in this fitted position. An example of the image captured using the PALM technique is shown in **Figure** 4 which compares the traditionally used com-

parative summed-molecule total internal reflection technique to the PALM technique. There is marked improvement in the image quality.

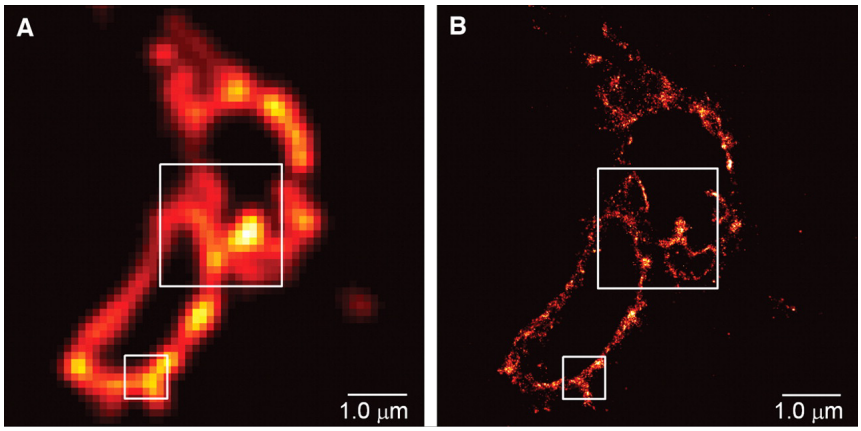

Figure 4: A sample image of proteins in a cell using (a) the traditionally used comparative summed-molecule total internal reflection and (b) the PALM technique from [https://doi.org/10.1126/science.1127344] [12]. Reprinted with permission from AAAS.

2.2.4 Quantum Super-Resolution Techniques

Other quantum-based imaging techniques such as optical centroid measurement (OCM) [14, 15, 16, 17, 18] or those using the anti-bunching effect [19, 20] have been applied to overcome the diffraction limit. The main limitation with these non-classical methods is the need for quantum low-brightness light sources such as single-photon sources or entangled photons. Another limitation is that they require high-order intensity correlation measurements. These additional limitations prevent them from widespread use in the real world.

OCM works by detecting the centroid of entangled bi-photons. As proposed by Tsang [14], images can be reconstructed using the intensity measurement of the light and post-processing using a Gaussian single-parameter estimation technique. In this case, the super-resolution ability comes from the OCM state of light carrying a spatial structure to allow it to overcome the Raleigh limit. In this technique, the laser source illuminates the object, which is then imaged by a 4f system. At the focus of the 4f system is a nonlinear crystal, which produces the photon pairs through spontaneous parametric down-conversion. A bandpass filter transmits these photon pairs, which are then focused with a lens onto a camera at the image plane. An example of this technique is shown in **Figure 5** [21].

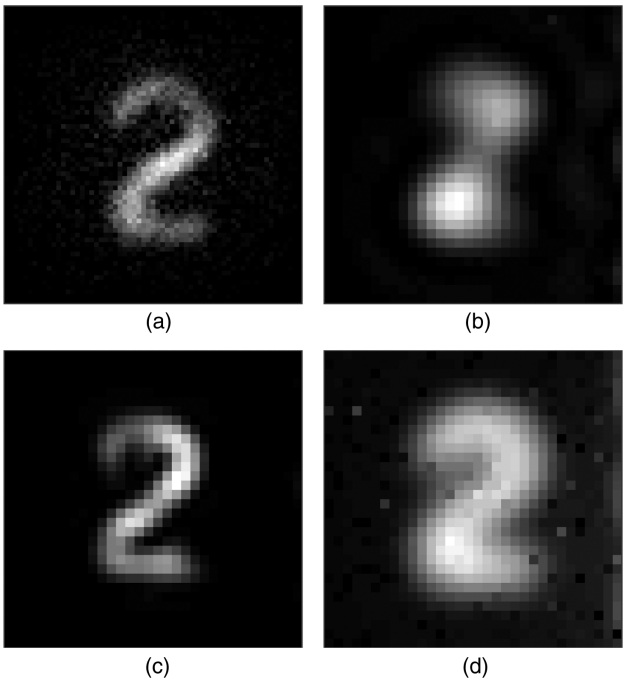

Figure 5: Images of a 2, taken using various methods (a) Bi-photon OCM at 810 nm, (b) spatially coherent 810 nm, (c) spatially coherent 405 nm, and (d) spatially incoherent 810 nm, reprinted with permission from [https://doi.org/10.1364/OPTICA.5.001150] [21] © The Optical Society. Note that the biphoton OCM comes from 405 nm light incident on a nonlinear crystal to create two 810 nm photons.

The anti-bunching effect operates on the principle that a single emitter can only emit one photon at a time. It is particularly useful for characterizing single quantum systems through quantum correlation measurements. In this case, [20] fluorophores are used where the emission of more than one photon is suppressed. This is the case for many organic dyes or fluorescent quantum dots. Staining a sample with these fluorescent dots and then scanning the sample and measuring quantum correlations allows for a significant increase in resolution compared to traditional scanning microscopy [19].

2.2.5 Spatial Mode Demultiplexing

Recently, a quantum-inspired super-resolution imaging method was proposed by Tsang [22] and demonstrated [23, 24, 25, 26, 27]. Although quantum-inspired, it does not require the use of non-classical light sources or high-order coincidence detection, giving it an advantage over previous quantum methods. This method, named SPADE for spatial mode demultiplexing, is based on spatial mode sorting. It is possible to resolve the two spatially incoherent, equally bright point sources regardless of their separation, which can be made arbitrarily small. This is done by sorting into an appropriate spatial mode basis and using photon counting statistics. SPADE approaches resolving the point sources as a parameter estimation problem. This works well for a small number of point objects but quickly becomes non-trivial when

applied to general scenes due to the complexity of multi-parameter estimation problems [28, 29].

2.2.6 Theoretical Fisher Information

Some theoretical approaches for developing sorter-based 2D super-resolution have been described [30, 31, 29, 32, 33, 34, 35, 36, 37, 38]. However, these scenes treated only a small number of unknown parameters because they focused mainly on Fisher information, which quickly becomes computationally complex as the number of parameters increases.

2.2.7 Motivation

After reviewing the existing literature, to the best of our knowledge, a mode sorter has not been used to super-resolve an arbitrary object. Consequently, our work focused on utilizing a mode sorter for super-resolution by treating resolving an image as a deconvolution problem. As described in more detail in Section 2.3, we propose to use the standard confocal microscopy setup, with a spatial mode sorter replacing the pinhole. We also generalized the standard Richardson-Lucy (RL) deconvolution algorithm [39, 40] to process the multiple outputs from the mode sorter. Together, these two techniques yield a reconstructed super-resolved image.

2.3 Methods

This section describes the choice of algorithm, mode-sorting bases, images and the units for their quality measurement, and the cut-off points for the iterative process used in the technique in the accompanying paper. In addition, more detailed descriptions of the methods may be found in Section 2.5.

2.3.1 Richardson-Lucy Deconvolution Algorithm

The Richardson-Lucy (RL) algorithm is a commonly used deconvolution algorithm described by **Equation 3** [39, 40], where W_r is the deconvolved image at the r-th iteration, M is the PSF of the conventional confocal imaging system with a pinhole and I_{con}^{exp} is the resultant confocal image. It has been combined with other techniques to perform deconvolution in 3D confocal microscopy [41]. In fact, in a comparison between multiple iterative algorithms (the iterative constrained Tikhonov–Miller algorithm (ICTM), the Carrington algorithm, and the RL algorithm with Gaussian prefiltering) the RL algorithm performed the best in low light scenarios of image restoration [42]. In our model, we are considering only the fundamental quantum noise, which can be described using Poissonian photon statistics as this is representative of

the noise when imaging with a laser beam. Indeed, the RL algorithm has been found to perform well in cases when the dominant noise is of a clear Poissonian nature [43, 42].

Ultimately, the RL algorithm shown in **Equation 3** is a well-known deconvolution algorithm commonly used for image reconstruction and applied to confocal microscopy. It is also simple and easily generalized to the multi-mode case in **Equation 4**.

$$W_{r+1} = W_r \cdot \left(M * \frac{I_{\text{con}}^{\text{exp}}}{M * W_r} \right), \tag{3}$$

$$W_{r+1} = W_r \cdot \sum_{mn} \left(Q_{mn} * \frac{H_{mn}^{\text{exp}}}{Q_{mn} * W_r} \right). \tag{4}$$

For the mode sorter case Q_{mn} is the PSF for the Zernike mode (Z_{mn}) imaging system and H_{mn}^{exp} is the image seen in that mode (after raster scanning). It is important to note that there is no weighting factor for each mode. We tested having different weights for each mode but after observing no significant difference, we opted to keep the weighting factor equal to 1. In doing so, the weighting is essentially based on how many photons appear in each mode, since we do not normalize them individually. We believe this is a reasonable way to weight the images since it accurately reflects the information in each mode. A more in-depth explanation can be found in the paper itself.

2.3.2 Zernike Modes

In the spatial-mode demultiplexing (SPADE) technique described in Section 2.2, the mode sorter used the Hermite-Gauss (HG) basis [22]. Initially, we also employed an HG basis. However, it has been shown that the optimal basis for an imaging system with a circular aperture, as in confocal microscopy, is the Zernike basis [31, 44]. Theoretically, one could sort the light into an infinite number of modes in the HG basis or sort the light into an infinite number of modes in the Zernike basis and gather all of the necessary information. In our case, an optimal will be the one that requires the fewest modes to capture the most light and most information. Consequently, we decided to employ the first six Zernike modes, since additional modes did not increase the reconstructed image quality and only increased the computation time. However, using fewer modes was detrimental to the image reconstruction.

2.3.3 Mode Sorting

The use of a spatial mode sorter instead of the traditional pinhole is a key component of our super-resolution method. This is described in more detail in the manuscript presented in Section 2.5 under **2. Generalized Richardson-Lucy deconvolution algorithm** as well as in Section 2. of the supplemental document.

A simple explanation of the simulated projection is as follows. The 2D image H_{mn} is produced by raster scanning the object. As we raster scan, each point is treated as a point source located at this specific coordinate. This electric field of the point source after our imaging system, i.e. in the Fourier plane, is projected onto the Zernike mode Z_n^m by calculating the overlap integral between the two fields. Now while our work was theoretical, Tsang's proposed experimental approach [22] relies on a multi-mode waveguide that uses a grating coupler to separate the different spatial modes, or alternatively evanescent coupling to single-mode waveguides. At the end of the multi-mode waveguide a photon counter will count the higher order photons that remain.

2.3.4 Images

As this is a theoretical simulation, the algorithm was tested with a series of images to assess the performance. We offer an example here that is different from the patterns discussed in the manuscript. In **Figure 6** we see an original pinwheel image (a) that has been conventionally reconstructed (b), a blurred (c) (i.e. with no reconstruction) image, and a mode sorter reconstructed image (d). This was for the typical configuration used, for an 80-pixel Rayleigh criterion resolution (an input in our algorithm which represents the limit such that features smaller than this will not be resolved) and, in this case, a photon number of $N_T = 10^7$. Recall that the goal is to be able to apply this to general and unknown images so it is important to be able to image various types of scenes.

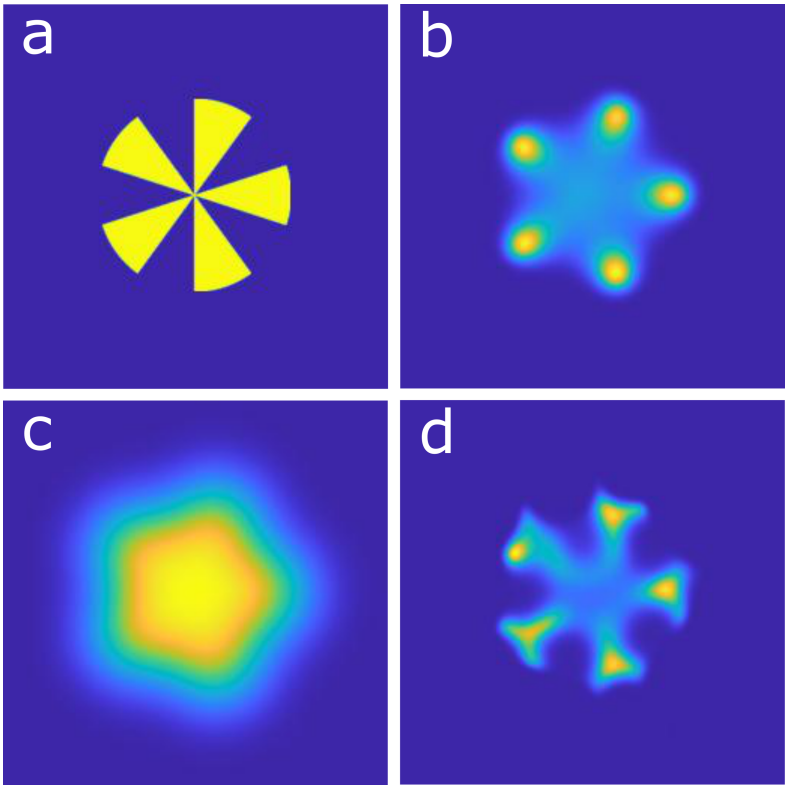

Figure 6: A pinwheel is imaged under the following conditions (a) original, (b) conventionally reconstructed, (c) blurred, i.e., no reconstruction, and (d) mode sorter reconstructed. This was for the typical configuration used, for an 80-pixel Rayleigh resolution with a photon number of $N_T = 10^7$.

2.3.5 Resolution Enhancement

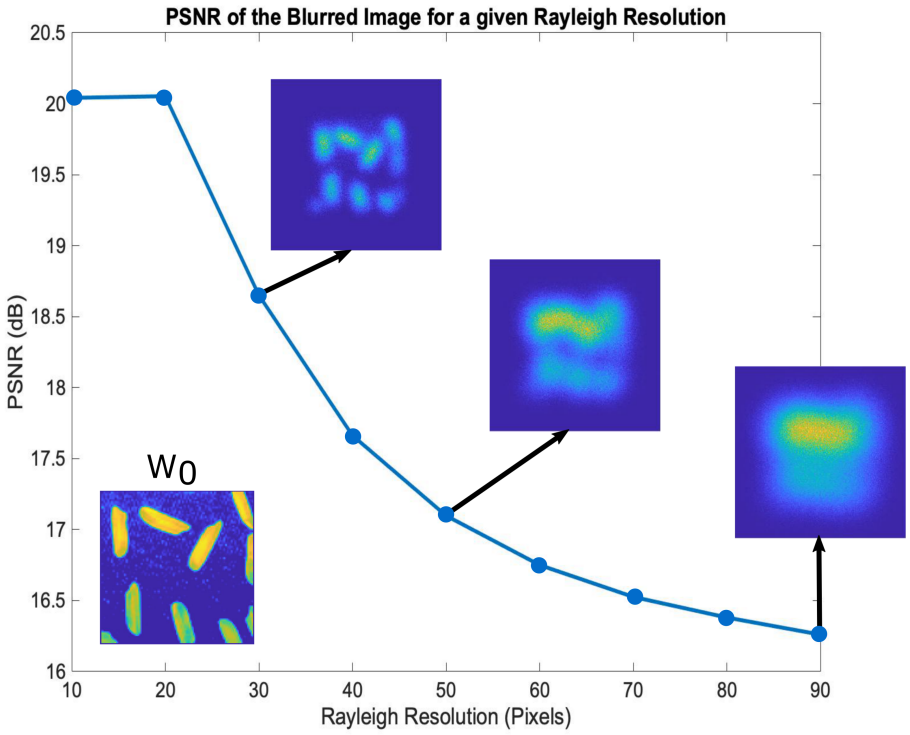

Figure 7: To give a quantitative description of the resolution enhancement, a relationship between the PSNR and the Rayleigh resolution is calculated by blurring the image at various Rayleigh resolutions and calculating the PSNR. Examples of the blurred and original rice image are shown to illustrate this point.

The peak signal-to-noise ratio (PSNR) is a commonly used measurement to compare image (W_r) quality based on the ground truth (W_0). The definition of PSNR is given by [45]

$$\mathrm{PSNR} = 10\log_{10}\frac{\max(W_0)^2}{\frac{1}{N^2}\sum_{i=1}^{N}\sum_{j=1}^{N}|W_0(i,j)-W_r(i,j)|^2}, \tag{5}$$

where (i, j) are the integer pixel indices of the digital image. In our case, the number of pixels along one dimension is $N = 256$. However, for super-resolution methods, people often ask: What is the "resolution enhancement"? To address this question we derived a relationship between the PSNR and the resolution enhancement by blurring the ground truth at various Rayleigh resolutions using the PSF of the imaging system for a specific Rayleigh criterion (resolution). The PSNR of this blurred image was then calculated so each Rayleigh resolution had a corresponding PSNR. Working this relationship backwards, we were able to determine a PSNR of our image that was equivalent to a given Rayleigh resolution. The ratio of the calculated Rayleigh resolution to the ground truth Rayleigh resolution gives the effective resolution enhancement. **Figure 7** gives an example of this calculation for the MatLab rice image. It is important

to note that this PSNR to resolution curve will be different for each individual image.

2.3.6 Iterative Stopping Criterion

In our numerical simulations, we allowed the algorithm to run until it reached a maximum iteration number limited by our computational and time constraints. Because we knew the ground truth we were able to compare the PSNRs at each iteration and choose the iteration with the maximum PSNR. However, without knowledge of the ground truth, it is not possible to do this, and therefore a stopping criterion must be chosen [46]. The simplest criterion would be a pre-selected iteration number to serve as the cut-off. To determine what that ideal iteration number might be, a series of simulations were conducted at varied total photon numbers. This is shown in Figure 4 of the Supplemental Document (Section 2.5), in the accompanying publication. As the photon numbers increase, we observe a saturation effect in the value of the PSNR as the iteration number increases. Overall, it is best to choose a lower iteration number when the photon number is lower $< 10^7$ as the image tends to improve quickly and additional iterations cause a degradation in resolution. It is better to use a higher number of iterations (reaching the saturation point) when the photon number is higher $> 10^8$ as the images continue to improve with more iterations.

2.4 Conclusion and Future Work

In conclusion, our simulations demonstrate that we are able to achieve super-resolution by applying a generalized Richardson-Lucy algorithm to a sorter-based confocal microscope. Our algorithm can resolve general images using a spatial mode sorter, which has not been previously demonstrated in literature. For both patterns tested, the average effective resolution enhancement for the sorter-based approach over 30% higher than the conventional confocal approach.

As previously mentioned in Section 2.2, there are many different techniques used to achieve image super-resolution in microscopy. Often, multiple resolution enhancing methods are used together to achieve the maximum possible resolution improvement. Given the simplicity of our generalized algorithm, it would be well suited to integration with other methods. Additionally, it does not require a quantum light source such as single photons (sensitive to loss) or photon pairs (require external delays and correlation measurements). Our method is applicable in cases where classical light is used, e.g., astronomical or fluorescence imaging. Having demonstrated that our algorithm can resolve general scenes, one potential application for this approach would be super-resolving digits, where our algorithm would be the front-end to a machine learning-based digit identification protocol [47]. Looking forward, we could

also consider whether the RL algorithm is indeed the best algorithm to process the mode sorter outputs or if a machine learning approach might yield a better resolution enhancement than the RL algorithm.

2.5 Publication: Confocal Super-Resolution Microscopy Based on a Spatial Mode Sorter

Research Article | Vol. 29, No. 8 / 12 April 2021 / Optics Express 11784
Optics EXPRESS

Confocal super-resolution microscopy based on a spatial mode sorter

KATHERINE K. M. BEARNE,[1,7] YIYU ZHOU,[2,7,*] BORIS BRAVERMAN,[1] JING YANG,[3] S. A. WADOOD,[2] ANDREW N. JORDAN,[3,4] A. N. VAMIVAKAS,[2,3,5] ZHIMIN SHI,[6] AND ROBERT W. BOYD[1,2,3]

[1]*Department of Physics, University of Ottawa, Ottawa, Ontario K1N 6N5, Canada*
[2]*The Institute of Optics, University of Rochester, Rochester, New York 14627, USA*
[3]*Department of Physics and Astronomy, University of Rochester, Rochester, New York 14627, USA*
[4]*Institute for Quantum Studies, Chapman University, Orange, California 92866, USA*
[5]*Materials Science Program, University of Rochester, Rochester, New York 14627, USA*
[6]*Department of Physics, University of South Florida, Tampa, Florida 33620, USA*
[7]*These authors contributed equally*

Abstract: Spatial resolution is one of the most important specifications of an imaging system. Recent results in the quantum parameter estimation theory reveal that an arbitrarily small distance between two incoherent point sources can always be efficiently determined through the use of a spatial mode sorter. However, extending this procedure to a general object consisting of many incoherent point sources remains challenging, due to the intrinsic complexity of multi-parameter estimation problems. Here, we generalize the Richardson-Lucy (RL) deconvolution algorithm to address this challenge. We simulate its application to an incoherent confocal microscope, with a Zernike spatial mode sorter replacing the pinhole used in a conventional confocal microscope. We test different spatially incoherent objects of arbitrary geometry, and we find that the resolution enhancement of sorter-based microscopy is on average over 30% higher than that of a conventional confocal microscope using the standard RL deconvolution algorithm. Our method could potentially be used in diverse applications such as fluorescence microscopy and astronomical imaging.

1. Introduction

Enhancing spatial resolution is a persistent goal for imaging systems. The resolution of an incoherent far-field imaging system was previously believed to be limited by Rayleigh's criterion [1]. In recent decades, a multitude of super-resolution methods have been demonstrated to break the diffraction limit, such as stimulated-emission depletion (STED) [2], photoactivated localization microscopy (PALM) [3], and stochastic optical reconstruction microscopy (STORM) [4]. However, these methods generally require the use of specially prepared fluorescent molecules, and the data collection in an experiment can take a long time. In addition to these classical methods, various quantum effects have been investigated to enhance the imaging resolution. Optical centroid measurement [5–9] is another quantum approach that can improve the resolution by up to 41% via detecting the centroid of entangled bi-photons. The anti-bunching effect has also been exploited to enhance the spatial resolution when imaging single-photon sources such as quantum dots through the use of coincidence measurement [10,11]. Nonetheless, these non-classical methods typically require the use of quantum, low-brightness light sources (e.g., single-photon sources and entangled-photon sources) as well as slow, high-order intensity correlation measurements, which limits their widespread adoption in real-world imaging systems.

#419493 https://doi.org/10.1364/OE.419493
Journal © 2021 Received 12 Jan 2021; revised 10 Mar 2021; accepted 24 Mar 2021; published 31 Mar 2021

Optics EXPRESS

In recent years, a quantum-inspired super-resolution imaging method based on spatial mode sorting (called SPADE) has been proposed [12] and experimentally demonstrated [13–17]. The Rayleigh diffraction limit can be broken through the use of an appropriate spatial mode sorter, and an arbitrarily small separation between two spatially incoherent, equally bright point sources can be well resolved. Although the theory for SPADE was developed in the framework of quantum metrology, it can be interpreted classically [18] and does not need non-classical light sources or high-order coincidence detection, which is the major advantage over the aforementioned super-resolution methods. The theoretical treatment of SPADE approaches the super-resolution task as a parameter estimation problem, which works well when imaging a scene with a small number of point objects. However, it is non-trivial to apply the theory to a general scene that contains many point sources or continuous objects due to the complexity of multi-parameter estimation problems [19,20]. A few theoretical attempts have been made towards sorter-based super-resolution imaging for a scene with a very small number of unknown parameters [20–29]. However, these previous works mainly focus on the Fisher information analysis of the mode sorter, which exhibits intractable complexity in the calculation of quantum Fisher information. Furthermore, even if the quantum Fisher information can be computed, it is challenge to determine if the quantum Fisher information can be achieved by practical measurements for all parameters. Hence, to the best of our knowledge, no method has yet been reported to super-resolve an object of arbitrary geometry using a mode sorter. Here we address this challenge by treating the sorter-based super-resolution imaging as a deconvolution problem. We propose to replace the pinhole in a standard confocal microscope with a spatial mode sorter. We generalize the standard RL deconvolution algorithm [30,31] to digitally process the multiple outputs of the mode sorter in order to reconstruct a super-resolved image. In Section 2, we introduce the conceptual schematic of the sorter-based confocal microscopy as well as the algorithm for image reconstruction. In Section 3, we present the numerical simulation results. The conclusion of this work is discussed in Section 4.

2. Generalized Richardson-Lucy deconvolution algorithm

The schematic of a confocal microscope is shown in Fig. 1(a) and (b). Conventional confocal microscopy uses a pinhole in the image plane before the single-pixel detector. Here we assume that the illumination beam is spatially coherent and the light scattered by the object is spatially incoherent, which is common in fluorescence microscopy. The illumination and reflected beam wavelengths are assumed to be the same for simplicity, although they can be different in fluorescence microscopy. We use W_0 to describe the object brightness profile and use M to denote the point spread function (PSF) of the conventional confocal microscope using a pinhole of diameter D. Here we assume a circular aperture of the objective lens, and the PSF of the objective lens is thus an Airy disk [32]. Additional details of M are presented in Supplement 1. By raster scanning the object, a 2D image can be obtained, and the resultant confocal image I_{con} can be described by the convolution of W_0 and M as $I_{\mathrm{con}} = M * W_0$. In our model we consider only the fundamental quantum noise which leads to Poissonian photon statistics; we ignore other technical sources of noise. Therefore, the shot-noise-limited image that can be experimentally measured is described by $I_{\mathrm{con}}^{\mathrm{exp}} = \mathrm{Poisson}(I_{\mathrm{con}})$, where $\mathrm{Poisson}(\cdot)$ denotes one random realization of the Poisson distribution for a given mean. The standard RL deconvolution algorithm can be expressed as [30,31]

$$W_{r+1} = W_r \cdot \left(M * \frac{I_{\mathrm{con}}^{\mathrm{exp}}}{M * W_r} \right), \tag{1}$$

where W_r is the deconvolved image in the r-th iteration and $*$ denotes convolution. In general, the iterative deconvolution algorithm begins with an image of uniform intensity $W_{r=1} = \mathrm{const}$, and the term inside the parentheses in the above equation can be understood as a correction to W_r during each iteration. The proposed sorter-based confocal microscope is shown in Fig. 1(b). It

Optics EXPRESS

can be seen that a Zernike mode sorter is used in the Fourier plane. Here Zernike modes are adopted because they have been shown to be the optimal basis for an imaging system with a circular aperture [22,33]. In particular, we choose the six lowest-order Zernike modes (Z_0^0, Z_1^{-1}, Z_1^1, Z_2^{-2}, Z_2^0, and Z_2^2), as shown in Fig. 1(c). The Zernike mode sorter projects the collected photons onto each Zernike mode Z_n^m in the Fourier plane, and each output port of the Zernike mode sorter produces a 2D image H_{mn} by raster scanning the object. The image H_{mn} is given by the convolution of the original object image W_0 and Q_{mn} as $H_{mn} = W_0 * Q_{mn}$, where Q_{mn} is the effective PSF when projecting into the mode Z_n^m:

$$\begin{aligned} Q_{mn}(x_1, y_1) &= N_0 \frac{k^2 \mathrm{NA}^2}{4\pi} B_{m=0,n=0}(r_1, \theta_1) \cdot B_{mn}(r_1, \theta_1), \\ B_{mn}(r_1, \theta_1) &= \frac{8(n+1)}{\epsilon_m} \frac{J_{n+1}^2(k\mathrm{NA}r_1)}{(k\mathrm{NA}r_1)^2} \sin^2\left(m\theta_1 + \frac{\pi}{2} \cdot \mathcal{H}(m)\right), \end{aligned} \tag{2}$$

where $J_{n+1}(\cdot)$ is the Bessel function of order $n+1$; $\epsilon_m = 2$ if $m = 0$ and $\epsilon_m = 1$ if $m \neq 0$; $\mathcal{H}(m)$ is the Heaviside step function where $\mathcal{H}(m) = 1$ if $m \geqslant 0$ and $\mathcal{H}(m) = 0$ if $m<0$; (x_1, y_1) are the Cartesian coordinates at the object plane, and (r_1, θ_1) are the corresponding polar coordinates; N_0 is the photon number in the illumination beam at each raster scanning step; $k = 2\pi/\lambda$ is the wave number, λ is the wavelength, and NA is the collection numerical aperture of the objective lens. In this equation, $B_{m=0,n=0}$ represents the PSF of the illumination beam, and B_{mn} is the

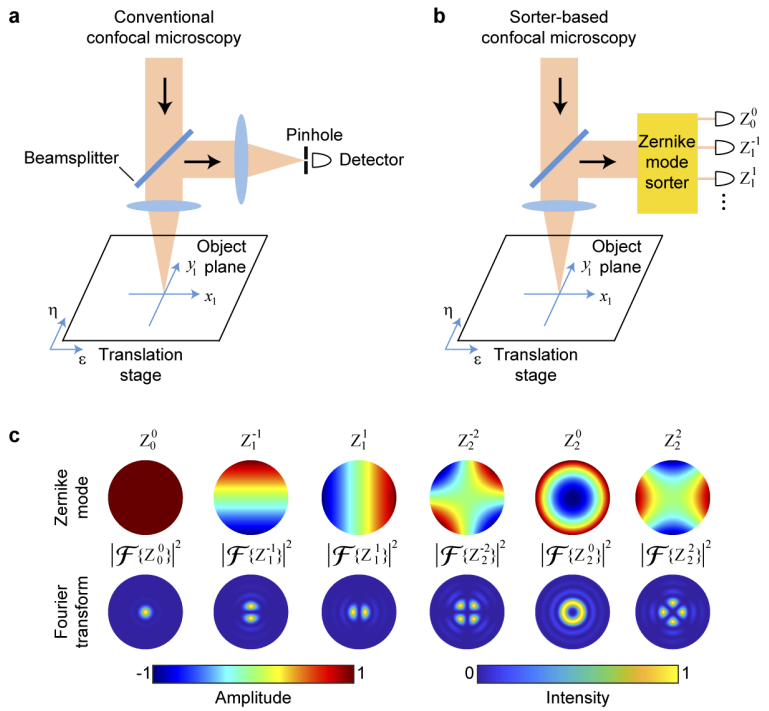

Fig. 1. (a) Schematic of a conventional confocal microscope. (b) Schematic of the sorter-based confocal microscopy. Conventional confocal microscopy uses a pinhole and a single detector, while the proposed scheme uses a spatial mode sorter to first decompose the received field, with every output port of the sorter measured by a separate detector. (c) The first six Zernike modes Z_n^m and the intensity profiles of their respective Fourier transforms $|\mathcal{F}\{Z_n^m\}|^2$.

Optics EXPRESS

intensity profile of the Fourier transform of Z_n^m in the image plane as shown in the bottom row in Fig. 1(c). Here, we assume that the illumination beam has a flat spatial profile before being focused by the objective lens and that the illumination NA is the same as the collection NA. We use this assumption to simplify the calculation and simulation, but we note that this assumption can be relaxed and is not necessary to the result. Derivations of the analytical form of B_{mn}, H_{mn} and Q_{mn} are presented in Supplement 1. We use $H_{mn}^{\exp} = \text{Poisson}(H_{mn})$ to denote the randomly generated shot-noise-limited image that can be measured in an experiment. As one can see, a major difference between the conventional confocal microscopy and the sorter-based confocal microscopy is that multiple images (six in our case) can be obtained simultaneously when using a mode sorter. Here we propose a generalized RL deconvolution algorithm, which can be expressed as

$$W_{r+1} = W_r \cdot \sum_{mn} \left(Q_{mn} * \frac{H_{mn}^{\exp}}{Q_{mn} * W_r} \right). \tag{3}$$

Compared to the conventional RL deconvolution algorithm (Eq. (1)), it can be seen that the correction term inside the parentheses in the above equation is the sum of contributions from different modes.

3. Numerical simulation

3.1. Algorithm performance evaluation

We next present the results of numerical simulations that implement the generalized deconvolution algorithm and compare its performance to that of the conventional deconvolution algorithm. One of the objects we use (pattern A) is shown in Fig. 2(a). The original object image has a size of 128×128 pixels and is zero padded to 256×256 pixels to avoid the diffraction-induced boundary clipping effect. A 2D image $H_{mn}^{\exp}$ can be obtained at each output port of the mode sorter when raster scanning the translation stage by (ϵ, η). Here we choose the scanning step size to be 1 pixel and the total scanning steps to be 256×256, resulting in a 2D image $H_{mn}^{\exp}(\epsilon, \eta)$ of 256×256 pixels. At each scanning step, we assume that N_0 photons are used to illuminate the object, and thus the total photon number in the illumination beam is $N_T = 256 \times 256 \times N_0$. In this work, we use N_T as a variable and perform simulations under different N_T. This is because N_T is typically controllable in an experiment by adjusting the illumination laser power and is independent of the sample properties. The results for different Zernike mode outputs are shown in Fig. 2(b)-(g). One can see that the output of high-order modes has a lower photon count and is thus more susceptible to Poisson noise. We use $W_{r=1} = \text{const}$ as the starting point and run the iterative deconvolution algorithm based on Eq. (3). We choose the commonly used peak signal-to-noise ratio (PSNR) to quantify the quality of the reconstructed image W_r. The definition of PSNR is given by [34]

$$\text{PSNR} = 10 \log_{10} \frac{\max(W_0)^2}{\frac{1}{N^2} \sum_{i=1}^{N} \sum_{j=1}^{N} |W_0(i,j) - W_r(i,j)|^2}, \tag{4}$$

where (i, j) are the integer pixel indices of the digital image and $N = 256$ is the pixel size along one dimension. We stop the deconvolution algorithm at a maximum iteration number $N_{\text{ite}} = 10^4$, which is limited by time and computational power constraints. In general, the PSNR increases with increasing iteration number r. However, if the data is noisy, the noise can be amplified when the iteration number is large, and thus the PSNR can decrease if r continues to increase. In our implementation, we monitor the PSNR as a function of the iteration r and choose the maximum PSNR for $1 \leqslant r \leqslant N_{\text{ite}}$ for each implementation. The reconstructed image is shown in Fig. 2(h). More details on the PSNR as a function of the iteration number are provided Supplement 1. For practical applications where the ground truth is not available, a stopping criterion [35] must be used. The simplest (and perhaps the most widely used) stopping criterion is to manually

Optics EXPRESS

specify a maximum iteration number. The relation between PSNR and the iteration number for both sorter-based deconvolution algorithm and the conventional deconvolution algorithm is presented in Supplement 1 to illustrate the effect of a manually specified stopping criterion. The results show that both the conventional and sorter-based deconvolution algorithms have a similar dependence on the iteration number, and thus the PSNR improvement is almost independent of the chosen stopping criterion.

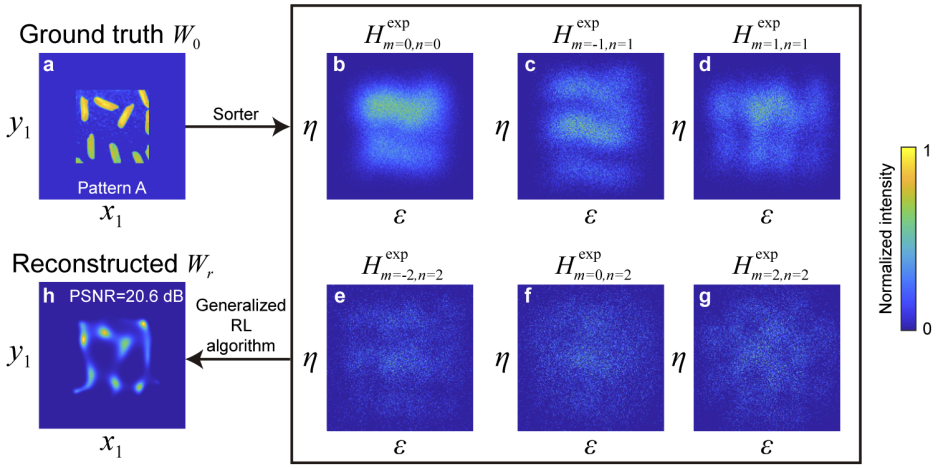

Fig. 2. Example of image reconstruction with the sorter-based super-resolution approach. (a) The ground truth image. (b-g) The 2D images H^{exp}_{mn} that can be measured via a Zernike mode sorter by raster scanning the ground truth image at the object plane in the presence of Poisson noise. (h) The reconstructed super-resolved image obtained by feeding the data H^{exp}_{mn} into the generalized RL deconvolution algorithm.

We next characterize the performance of the generalized deconvolution algorithm under different levels of Poisson noise by adjusting the total photon number N_T in the illumination beam. The ground truth for pattern A is shown in Fig. 3(a1), and we choose the Rayleigh-criterion resolution $\delta x_0 = 1.22\pi/(k\text{NA}) = 0.61\lambda/\text{NA}$ to be 80 pixels. We emphasize that only the relative ratio between λ/NA and the pixel pitch size is important, and here we do not specify the respective value of these parameters for generality. The noiseless, diffraction-limited confocal image without deconvolution I_{con} is shown in Fig. 3(a2), which is too blurry to reveal the details of the ground truth. We next vary the total photon number N_T and test the performance of the deconvolution algorithm with different N_T. The reconstructed images by the sorter-based deconvolution algorithm and the conventional deconvolution algorithm are presented in Fig. 3(a3)-(a6). We also test another pattern B made of four handwritten digits (MNIST handwritten digit database [36]) with non-uniform intensity profile as shown in Fig. 3(b1). The conventional confocal image I_{con} without deconvolution is shown in Fig. 3(b2), and the digits cannot be resolved based on this image. The sorter-based deconvolved images are presented in Fig. 3(b3) and (b5), and the conventional deconvolved images are presented in Fig. 3(b4,b6). It can be seen that the digits '0' and '1' using the sorter-based approach are more visually resolvable that the conventional deconvolved results. Figure 3(a7), (a8), (b7), and (b8) are 1D cross-sections through the images (indicated by the white bars), comparing the reconstructions to the ground truth. We can see how the reconstructions evolve as the photon number increases. At a larger photon number, the 1D cross-section shows a higher contrast and is more similar to the ground truth than at low photon numbers. In general, the sorter-based deconvolution algorithm provides a visibly higher

Optics EXPRESS

resolution as compared to the conventional deconvolution algorithm, in particular at a low total photon number.

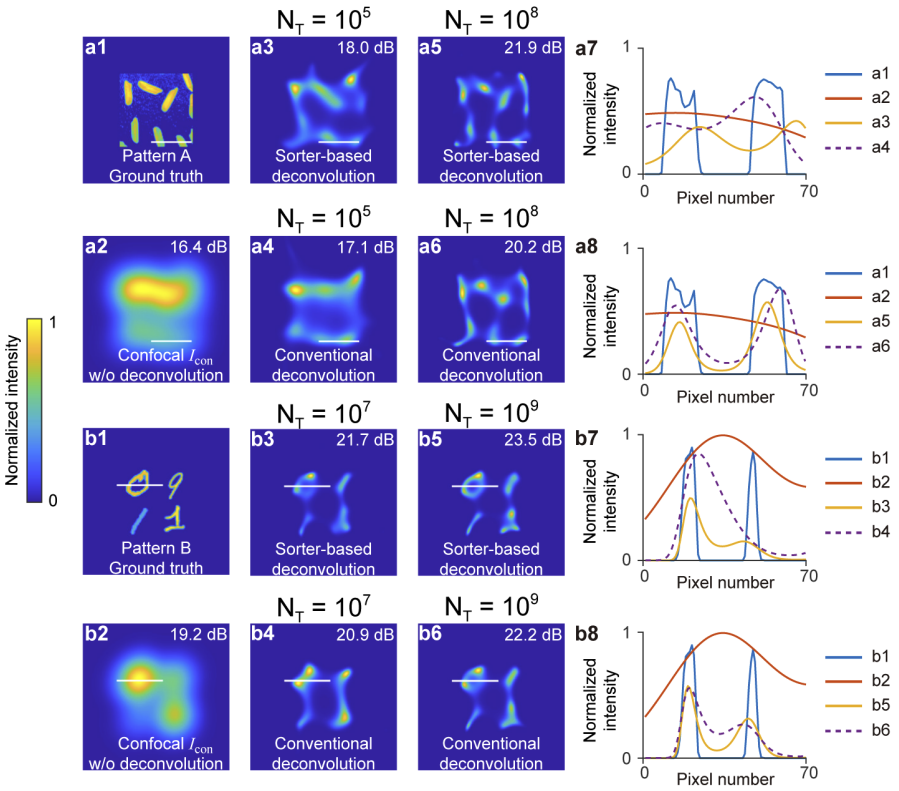

Fig. 3. (a1) Ground truth image for pattern A. (a2) The confocal diffraction-limited image without deconvolution. (a3-a6) The reconstructed images. The used algorithm and the total photon number N_T in the illumination beam are labeled near each image. (a7, a8) The 1D cross-section lines for (a1-a6) indicated by the corresponding white bars. (b1-b8) Results for pattern B. The PSNR is shown at the upper right corner of each image. In all 1D cross-section lines, it can be seen that the sorter-based deconvolution algorithm consistently shows better contrast and fidelity to the ground truth than the conventional deconvolution algorithm.

3.2. *Effective resolution enhancement*

In Fig. 4 we compare the performance of the conventional deconvolution algorithm to the generalized deconvolution algorithm in terms of PSNR under different N_T for patterns A and B. For each N_T, we run the simulation six times with randomly generated Poisson noise to obtain the mean and the standard deviation of the PSNR of the reconstructed images. It can be seen that the generalized deconvolution algorithm based on the mode sorter consistently provides higher PSNR than the conventional confocal approach. Also, the PSNR of the reconstructed image generally increases when N_T increases. Although PSNR is a widely used metric for quantifying the image quality, the PSNR of reconstructed images for different ground truths cannot be compared directly. In addition, the PSNR does not provide an intuitive understanding of the reconstructed resolution. We next translate PSNR to the effective resolution enhancement in order to answer the frequently asked question "what is the resolution enhancement of your super-resolution method?". For a

Optics EXPRESS

ground truth image W_0, we blur it with PSFs of different resolutions as $W_{\text{blur}} = W_0 * M(\delta x)$, where $M(\delta x)$ is the PSF of the conventional confocal microscopy given a particular Rayleigh resolution δx. We then numerically calculate the PSNR of W_{blur} using Eq. (4) to obtain the relation between resolution δx and PSNR, i.e. PSNR $= f(\delta x)$. Therefore, for each reconstructed image W_r, we can calculate its effective resolution based on its PSNR via $\delta x_{\text{eff}} = f^{-1}(\text{PSNR})$, where f^{-1} is the inverse function of f. Hence, the effective resolution enhancement (ERE) can be calculated as

$$\text{ERE} = \delta x_0 / \delta x_{\text{eff}}, \tag{5}$$

and this quantity is shown on the right-hand side axis in Fig. 4. It can be seen that at the maximum total photon number $N_T = 10^{10}$, the effective resolution enhancement of sorter-based approach is higher than 5.0 for both pattern A and B. We note that the objects used in our simulation have a relatively small space-bandwidth product [37] because of the limited computational power, which allows for relatively high resolution enhancement. Moreover, the effective resolution enhancement of the sorter-based approach is on average 38% and 30% higher than that of the conventional approach for pattern A and pattern B, respectively. We also test nine additional images which are shown in Supplement 1. It can be seen that the mode sorter can provide on average 24% higher resolution enhancement over the conventional approach for the nine additional objects. We believe that our method can be readily applied to confocal fluorescence microscopy by using a Zernike mode sorter, and the Zernike mode sorter can in principle be experimentally realized by the multi-plane light conversion [38]. Another potential application of our method is the astronomical imaging where the collected light field is spatially incoherent. However, since the confocal scheme cannot be used in astronomical imaging, the formulas developed here need to be adjusted accordingly to account for the non-confocal scheme used in astronomical imaging.

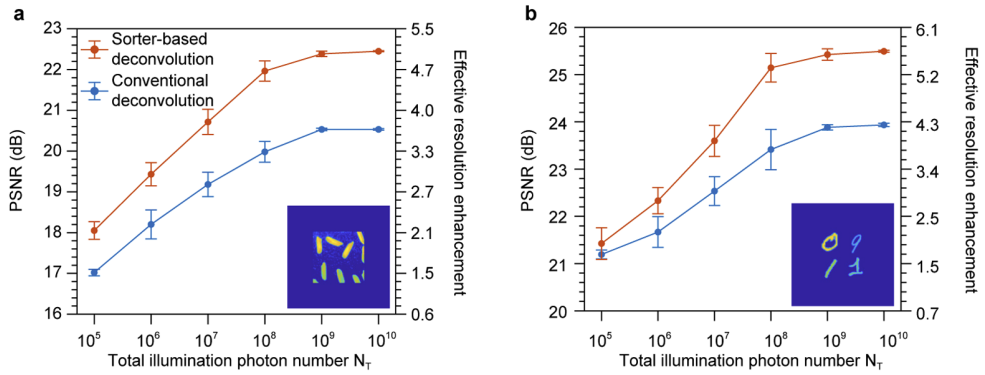

Fig. 4. The PSNR and effective resolution enhancement as functions of the total photon number N_T for (a) pattern A and (b) pattern B. Both the conventional deconvolution algorithm and the sorter-based deconvolution algorithm are tested for 6 reconstructions with randomly generated Poisson noise. The error bars represent the standard deviation of the PSNR of these trials. The inset shows the corresponding ground truth image.

4. Conclusion

In conclusion, we generalize the standard RL deconvolution algorithm and apply it to enhance the resolution of sorter-based confocal microscopy. We test our algorithm with general scenes, which has not previously been realized by spatial mode sorting, to the best of our knowledge. The effective resolution enhancement of the sorter-based approach can be as large as ≈5.6 when

Optics EXPRESS

the total photon number in the illumination beam is $N_T = 10^{10}$. For both patterns we test, the average effective resolution enhancement of the sorter-based approach is more than 30% higher that that of the conventional deconvolution algorithm. Hence, our generalized deconvolution algorithm can achieve robust super-resolution for general scenes compared to the conventional RL deconvolution algorithm. In particular, our generalized deconvolution algorithm allows for super-resolving strongly blurred images of digits, which could be used a front-end to a machine learning-based digit identification task [36]. Furthermore, our method does not require non-classical quantum light sources, and thus our generalized deconvolution algorithm can be potentially useful to applications such as fluorescence microscopy and astronomical imaging. Given the simplicity and generality of our generalized deconvolution algorithm, it is possible to integrate our method with existing quantum or classical super-resolution methods to increase the resolution even further.

Funding. National Science Foundation (OMA-1936321, 193632); Defense Advanced Research Projects Agency (D19AP00042); Canada Excellence Research Chairs, Government of Canada; Natural Sciences and Engineering Research Council of Canada; Banting Postdoctoral Fellowship; Universities Space Research Associates (SUBK-20-0002/08103.02); Office of Naval Research (N00014-17-1-2443).

Acknowledgments. Y.Z. acknowledges Mankei Tsang for helpful discussions.

Disclosures. The authors declare no conflicts of interest.

Supplemental document. See Supplement 1 for supporting content.

References

1. L. Rayleigh, "XXXI. Investigations in optics, with special reference to the spectroscope," Philos. Mag. Ser. **8**(49), 261–274 (1879).
2. S. W. Hell and J. Wichmann, "Breaking the diffraction resolution limit by stimulated emission: stimulated-emission-depletion fluorescence microscopy," Opt. Lett. **19**(11), 780–782 (1994).
3. E. Betzig, G. H. Patterson, R. Sougrat, O. W. Lindwasser, S. Olenych, J. S. Bonifacino, M. W. Davidson, J. Lippincott-Schwartz, and H. F. Hess, "Imaging intracellular fluorescent proteins at nanometer resolution," Science **313**(5793), 1642–1645 (2006).
4. M. J. Rust, M. Bates, and X. Zhuang, "Sub-diffraction-limit imaging by stochastic optical reconstruction microscopy (STORM)," Nat. Methods **3**(10), 793–796 (2006).
5. M. Tsang, "Quantum imaging beyond the diffraction limit by optical centroid measurements," Phys. Rev. Lett. **102**(25), 253601 (2009).
6. H. Shin, K. W. C. Chan, H. J. Chang, and R. W. Boyd, "Quantum spatial superresolution by optical centroid measurements," Phys. Rev. Lett. **107**(8), 083603 (2011).
7. L. A. Rozema, J. D. Bateman, D. H. Mahler, R. Okamoto, A. Feizpour, A. Hayat, and A. M. Steinberg, "Scalable spatial superresolution using entangled photons," Phys. Rev. Lett. **112**(22), 223602 (2014).
8. M. Unternährer, B. Bessire, L. Gasparini, M. Perenzoni, and A. Stefanov, "Super-resolution quantum imaging at the Heisenberg limit," Optica **5**(9), 1150–1154 (2018).
9. E. Toninelli, P.-A. Moreau, T. Gregory, A. Mihalyi, M. Edgar, N. Radwell, and M. Padgett, "Resolution-enhanced quantum imaging by centroid estimation of biphotons," Optica **6**(3), 347–353 (2019).
10. R. Tenne, U. Rossman, B. Rephael, Y. Israel, A. Krupinski-Ptaszek, R. Lapkiewicz, Y. Silberberg, and D. Oron, "Super-resolution enhancement by quantum image scanning microscopy," Nat. Photonics **13**(2), 116–122 (2019).
11. O. Schwartz, J. M. Levitt, R. Tenne, S. Itzhakov, Z. Deutsch, and D. Oron, "Superresolution microscopy with quantum emitters," Nano Lett. **13**(12), 5832–5836 (2013).
12. M. Tsang, R. Nair, and X.-M. Lu, "Quantum theory of superresolution for two incoherent optical point sources," Phys. Rev. X **6**(3), 031033 (2016).
13. F. Yang, A. Tashchilina, E. S. Moiseev, C. Simon, and A. I. Lvovsky, "Far-field linear optical superresolution via heterodyne detection in a higher-order local oscillator mode," Optica **3**(10), 1148–1152 (2016).
14. M. Paúr, B. Stoklasa, Z. Hradil, L. L. Sánchez-Soto, and J. Rehacek, "Achieving the ultimate optical resolution," Optica **3**(10), 1144–1147 (2016).
15. W.-K. Tham, H. Ferretti, and A. M. Steinberg, "Beating Rayleigh's curse by imaging using phase information," Phys. Rev. Lett. **118**(7), 070801 (2017).
16. Z. S. Tang, K. Durak, and A. Ling, "Fault-tolerant and finite-error localization for point emitters within the diffraction limit," Opt. Express **24**(19), 22004–22012 (2016).
17. Y. Zhou, J. Yang, J. D. Hassett, S. M. H. Rafsanjani, M. Mirhosseini, A. N. Vamivakas, A. N. Jordan, Z. Shi, and R. W. Boyd, "Quantum-limited estimation of the axial separation of two incoherent point sources," Optica **6**(5), 534–541 (2019).

Optics EXPRESS

18. M. Tsang, "Subdiffraction incoherent optical imaging via spatial-mode demultiplexing: Semiclassical treatment," Phys. Rev. A **97**(2), 023830 (2018).
19. F. Albarelli, J. F. Friel, and A. Datta, "Evaluating the Holevo Cramér-Rao bound for multiparameter quantum metrology," Phys. Rev. Lett. **123**(20), 200503 (2019).
20. M. Tsang, "Semiparametric estimation for incoherent optical imaging," Phys. Rev. Res. **1**(3), 033006 (2019).
21. S. Zhou and L. Jiang, "Modern description of Rayleigh's criterion," Phys. Rev. A **99**(1), 013808 (2019).
22. J. Yang, S. Pang, Y. Zhou, and A. N. Jordan, "Optimal measurements for quantum multiparameter estimation with general states," Phys. Rev. A **100**(3), 032104 (2019).
23. M. Tsang, "Subdiffraction incoherent optical imaging via spatial-mode demultiplexing," New J. Phys. **19**(2), 023054 (2017).
24. J. Řehaček, Z. Hradil, B. Stoklasa, M. Paúr, J. Grover, A. Krzic, and L. Sánchez-Soto, "Multiparameter quantum metrology of incoherent point sources: towards realistic superresolution," Phys. Rev. A **96**(6), 062107 (2017).
25. X.-M. Lu, H. Krovi, R. Nair, S. Guha, and J. H. Shapiro, "Quantum-optimal detection of one-versus-two incoherent optical sources with arbitrary separation," npj Quantum Inf. **4**(1), 64 (2018).
26. S. Prasad, "Quantum limited source localization and pair superresolution in two dimensions under finite-emission bandwidth," Phys. Rev. A **102**(3), 033726 (2020).
27. K. A. Bonsma-Fisher, W.-K. Tham, H. Ferretti, and A. M. Steinberg, "Realistic sub-Rayleigh imaging with phase-sensitive measurements," New J. Phys. **21**(9), 093010 (2019).
28. M. Tsang, "Efficient superoscillation measurement for incoherent optical imaging," arXiv:2010.11084 (2020).
29. L. Peng and X.-M. Lu, "Generalization of Rayleigh's curse on parameter estimation with incoherent sources," arXiv:2011.07897 (2020).
30. W. H. Richardson, "Bayesian-based iterative method of image restoration," J. Opt. Soc. Am. **62**(1), 55–59 (1972).
31. L. B. Lucy, "An iterative technique for the rectification of observed distributions," Astron. J. **79**, 745 (1974).
32. G. B. Airy, "On the diffraction of an object-glass with circular aperture," Trans. of the Cambridge Philosoph. Soc. **5**, 283–291 (1835).
33. Z. Yu and S. Prasad, "Quantum limited superresolution of an incoherent source pair in three dimensions," Phys. Rev. Lett. **121**(18), 180504 (2018).
34. K. Nasrollahi and T. B. Moeslund, "Super-resolution: a comprehensive survey," Mach. Vision Appl. **25**(6), 1423–1468 (2014).
35. T. Herbert, "Statistical stopping criteria for iterative maximum likelihood reconstruction of emission images," Phys. Med. Biol. **35**(9), 1221–1232 (1990).
36. Y. LeCun, L. Bottou, Y. Bengio, and P. Haffner, "Gradient-based learning applied to document recognition," Proc. IEEE **86**(11), 2278–2324 (1998).
37. M. Bertero and P. Boccacci, "Super-resolution in computational imaging," Micron **34**(6-7), 265–273 (2003).
38. G. Labroille, B. Denolle, P. Jian, P. Genevaux, N. Treps, and J.-F. Morizur, "Efficient and mode selective spatial mode multiplexer based on multi-plane light conversion," Opt. Express **22**(13), 15599–15607 (2014).

Supplemental Document

Optics EXPRESS

Confocal super-resolution microscopy based on a spatial mode sorter: supplement

KATHERINE K. M. BEARNE,[1,7] YIYU ZHOU,[2,7,*] BORIS BRAVERMAN,[1] JING YANG,[3] S. A. WADOOD,[2] ANDREW N. JORDAN,[3,4] A. N. VAMIVAKAS,[2,3,5] ZHIMIN SHI,[6] AND ROBERT W. BOYD[1,2,3]

[1]*Department of Physics, University of Ottawa, Ottawa, Ontario K1N 6N5, Canada*
[2]*The Institute of Optics, University of Rochester, Rochester, New York 14627, USA*
[3]*Department of Physics and Astronomy, University of Rochester, Rochester, New York 14627, USA*
[4]*Institute for Quantum Studies, Chapman University, Orange, California 92866, USA*
[5]*Materials Science Program, University of Rochester, Rochester, New York 14627, USA*
[6]*Department of Physics, University of South Florida, Tampa, Florida 33620, USA*
[7]*These authors contributed equally*
[redacted]

Supplement DOI: https://doi.org/10.6084/m9.figshare.14274665

Parent Article DOI: https://doi.org/10.1364/OE.419493

Confocal super-resolution microscopy based on a spatial mode sorter: Supplemental Document

This Supplemental Document presents the mathematical derivations of equations in the primary manuscript, the reconstructed images at different iteration numbers, and the performance characterization for additional objects.

1. DERIVATION OF EFFECTIVE PSF OF THE CONVENTIONAL MICROSCOPY

In a conventional confocal microscope, the Airy-disk-shaped PSF of the illumination beam $G(x_1, y_1)$ can be written as

$$G(x_1, y_1) = N_0 \left| J_1(k\mathrm{NA}r_1)/(\sqrt{\pi}r_1) \right|^2 \tag{S1}$$

where (x_1, y_1) are the Cartesian coordinates and (r_1, θ_1) are the corresponding polar coordinates in the object plane, NA is the numerical aperture, λ is wavelength, and $k = 2\pi/\lambda$ is the wave number. Here the total energy of the illumination beam is $\iint G(x_1, x_2)dx_1dx_2 = N_0$, and thus the illumination beam contains N_0 photons. It can be noticed that (see Eq. (2) in the manuscript):

$$G(x_1, y_1) = N_0 \frac{k^2\mathrm{NA}^2}{4\pi} B_{m=0,n=0}(r_1, \theta_1) \tag{S2}$$

To obtain a 2D image, one needs to raster scan the object. This 2D translation is denoted as (ϵ, η). The intensity profile of the object is denoted by $W_0(x_1, y_1)$. When the object is excited by the illumination beam, the excited intensity distribution at the object plane is $W_0(x_1 - \epsilon, y_1 - \eta)G(x_1, y_1)$. For the reflected beam, we assume the imaging system has a magnification of unity, and the intensity PSF at the image plane can be described as

$$\phi(x_2, y_2) = \left| J_1(k\mathrm{NA}r_2)/(\sqrt{\pi}r_2) \right|^2. \tag{S3}$$

where (x_2, y_2) are the Cartesian coordinates at the image plane, (r_2, θ_2) are the polar coordinates at the image plane, and the energy of $\phi(x_2, y_2)$ is normalized to unity as $\iint \phi(x_2, y_2)dx_2dy_2 = 1$. Hence, the resultant image at the image plane can be written as

$$F(x_2, y_2; \epsilon, \eta) = \iint dx_1dy_1\phi(x_2 - x_1, y_2 - y_1)W_0(x_1 - \epsilon, y_1 - \eta)G(x_1, y_1). \tag{S4}$$

In a conventional confocal microscope, we use a pinhole with diameter D at the image plane in front of a bucket detector to measure the photon number. For the conventional confocal microscopy simulation, we use a pinhole of diameter $D = \delta x_0$, which is commonly used in experiments [1]. Therefore, by raster scanning the object, a 2D image $I_{\mathrm{con}}(\epsilon, \eta)$ can be obtained by the bucket detector, which can be written as

$$\begin{aligned} I_{\mathrm{con}}(\epsilon, \eta) &= \iint_{r_2 \leqslant D/2} dx_2dy_2F(x_2, y_2; \epsilon, \eta) \\ &= \iint_{r_2 \leqslant D/2} dx_2dy_2 \iint dx_1dy_1\phi(x_2 - x_1, y_2 - y_1)W_0(x_1 - \epsilon, y_1 - \eta)G(x_1, y_1). \end{aligned} \tag{S5}$$

Here we define

$$S(x_1, y_1) = \iint_{r_2 \leqslant D/2} dx_2dy_2\phi(x_2 - x_1, y_2 - y_1). \tag{S6}$$

Hence, the expression for $I_{\mathrm{con}}(\epsilon, \eta)$ can be rewritten in the form of a convolution as

$$\begin{aligned} I(\epsilon, \eta) &= \iint dx_1dy_1S(x_1, y_1)G(x_1, y_1)W_0(x_1 - \epsilon, y_1 - \eta) \\ &= \iint dx_1dy_1M(x_1, y_1)W_0(x_1 - \epsilon, y_1 - \eta) \\ &= M * W_0, \end{aligned} \tag{S7}$$

where

$$M(x_1, y_1) = S(x_1, y_1)G(x_1, y_1). \tag{S8}$$

2. DERIVATIONS OF EFFECTIVE PSF OF THE MODE SORTER-BASED MICROSCOPY

For our sorter-based method, we use a Zernike mode sorter to perform spatial mode decomposition. The expression for the normalized Zernike modes in the Fourier plane is

$$Z_n^m(r_p,\theta_p) = \sqrt{\frac{2(n+1)}{\epsilon_m \pi}} R_n^{|m|}(r_p)\sin(m\theta_p + \frac{\pi}{2}\cdot\mathcal{H}(m)), \tag{S9}$$

where (r_p,θ_p) are the scaled, dimensionless polar coordinates at the Fourier plane with $0 \leqslant r_p \leqslant 1$; $\epsilon_m = 2$ if $m = 0$ and $\epsilon_m = 1$ if $m \neq 0$; $\mathcal{H}(m)$ is the Heaviside function where $\mathcal{H}(m) = 1$ if $m \geqslant 0$ and $\mathcal{H}(m) = 0$ if $m < 0$; $R_n^{|m|}$ is the radial polynomial [2]. Consider a point source located at (x_1, y_1). Then the electric field on the scaled pupil plane is $\frac{1}{\sqrt{\pi}}\exp(ik\mathrm{NA}(x_1x_p + y_1y_p))$, where (x_p, y_p) is the dimensionless Cartesian coordinate at the Fourier plane with $x_p^2 + y_p^2 \leqslant 1$. In the polar coordinate, this field can be rewritten as $\frac{1}{\sqrt{\pi}}\exp(ik\mathrm{NA}r_1r_p\cos(\theta_1-\theta_p))$. Now we project this field to the Zernike modes $Z_n^m(r_p,\theta_p)$, and the overlap integral is [2]

$$\begin{aligned} B_{mn}(x_1,y_1) &= \left|\int_0^1 r_p dr_p \int_0^{2\pi} d\theta_p \frac{1}{\sqrt{\pi}}\exp(ik\mathrm{NA}r_1r_p\cos(\theta_1-\theta_p))\cdot Z_n^m(r_p,\theta_p)\right|^2 \\ &= \frac{8(n+1)}{\epsilon_m}\frac{J_{n+1}^2(k\mathrm{NA}r_1)}{(k\mathrm{NA}r_1)^2}\sin^2(m\theta_1 + \frac{\pi}{2}\cdot\mathrm{H}(m)). \end{aligned} \tag{S10}$$

It can be seen that the overlap integral coincides with the Fourier transform of Zernike modes. Therefore, when the object $W_0(x_1-\epsilon, y_1-\eta)$ is excited by the illumination beam $G(x_1,y_1)$, the sorter output is

$$\begin{aligned} H_{mn}(\epsilon,\eta) &= \iint dx_1dy_1 B_{mn}(x_1,y_1)G(x_1,y_1)W_0(x_1-\epsilon,y_1-\eta) \\ &= \iint dx_1dy_1 Q_{mn}(x_1,y_1)W_0(x_1-\epsilon,y_1-\eta) \\ &= Q_{mn} * W_0, \end{aligned} \tag{S11}$$

where

$$\begin{aligned} Q_{mn}(x_1,y_1) &= B_{mn}(x_1,y_1)\cdot G(x_1,y_1) \\ &= N_0\frac{k^2\mathrm{NA}^2}{4\pi}B_{m=0,n=0}(x_1,y_1)\cdot B_{mn}(x_1,y_1). \end{aligned} \tag{S12}$$

3. QUALITY OF ITERATIVE RECONSTRUCTIONS

We allow the algorithm to run until it reaches a maximum iteration number $N_{\text{ite}} = 10^4$, which is limited by time and computational power constraints. We monitor the PSNR at each iteration r and choose the maximum PSNR for $1 \leqslant r \leqslant N_{\text{ite}}$ for each implementation. In general, the PSNR increases with increasing iteration number r, as shown in Fig. S1(h). However, noisy data can cause the PSNR to decrease with increasing r, as the noise can be amplified when the iteration number is large. This effect is shown in Fig. S1(d). In Fig. S1(a-c) we see the progression of the image quality as the iteration number is increased. Fig. S1(e-g) illustrates the same progression when the total photon number N_T in the illumination beam increases. These images are reconstructions of pattern A.

In practical applications where the ground truth is unavailable, a stopping criterion is needed to stop the iterative algorithm. The simplest (and perhaps the most widely used) stopping criterion is to manually specify a maximum iteration number. To illustrate the effect of the manually specified stopping criterion, we show the relation between the PSNR and the iteration number for the conventional deconvolution algorithm and the sorter-based deconvolution algorithm with different N_T in Fig. S2. For each N_T, we generate six shot-noise-limited images with randomly generated Poisson noise. Therefore, we have 12 curves in each graph in total. It can be seen that the sorter-based deconvolution algorithm outperforms the conventional deconvolution algorithm for an arbitrary iteration number. To achieve the optimal performance, the user should choose a smaller iteration number when N_T is small. The results also show that both the conventional and sorter-based deconvolution algorithms have a similar dependence on the iteration number, and thus the PSNR improvement is almost independent of the chosen stopping criterion.

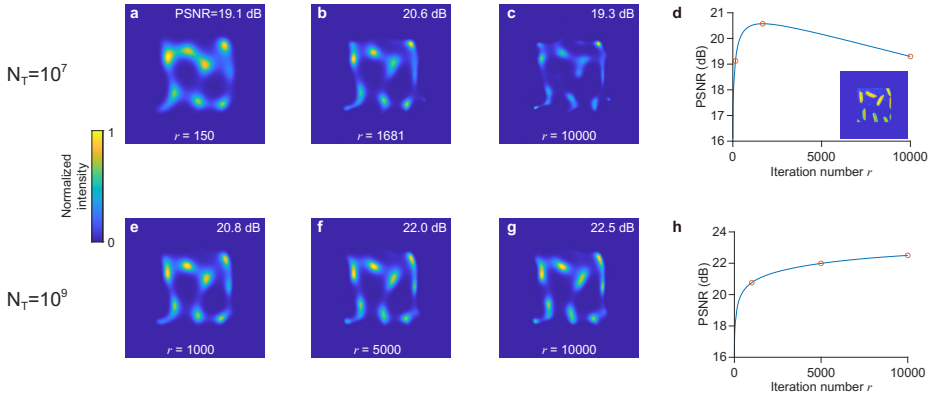

Fig. S1. (a-c) The reconstructed image at different iteration numbers by the sorter-based method when the total photon number $N_T = 10^7$. The corresponding PSNR as a function of iteration number r is shown in (d). The noise in the image can be amplified when the iteration number exceeds the optimal value. The inset shows the ground truth image. (e-g) The reconstructed image at different iteration numbers by the sorter-based method when the total photon number $N_T = 10^9$. The corresponding PSNR as a function of iteration number r is shown in (h).

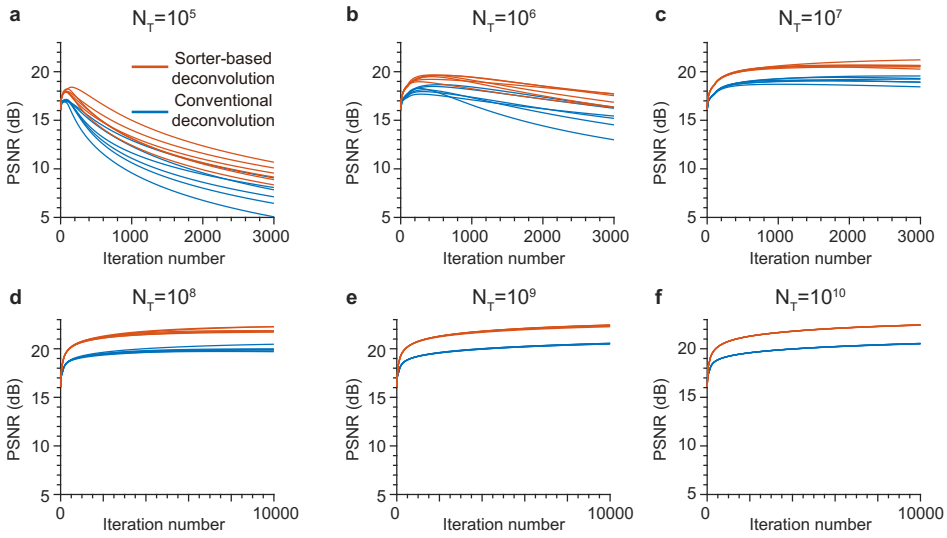

Fig. S2. The relation between the PSNR and the iteration number with different N_T for the conventional and sorter-based deconvolution algorithm. The value of N_T is shown on the top of each graph.

4. PERFORMANCE CHARACTERIZATION FOR ADDITIONAL IMAGES

The main goal of our approach is to super-resolve an object of arbitrary geometry using a mode sorter, as to the best of our knowledge this has not yet been accomplished. In order to test our algorithm, we fed it many images to reconstruct. In Fig. S3 we compare the performance of the conventional algorithm to the generalized algorithm in terms of PSNR and the effective resolution enhancement (ERE). Among all the data points shown in the inset of Fig. S3 (a-i), the PSNR enhancement $\mathrm{PSNR}_{\mathrm{sorter}} - \mathrm{PSNR}_{\mathrm{conventional}}$ has a minimum value of 0.17 dB, a maximum value of 1.73 dB, and an average value of 0.82 dB. The effective resolution enhancement ratio $\mathrm{ERE}_{\mathrm{sorter}} / \mathrm{ERE}_{\mathrm{conventional}}$ has a minimum value of 107%, a maximum value of 150.5%, and an average value of 124.2%.

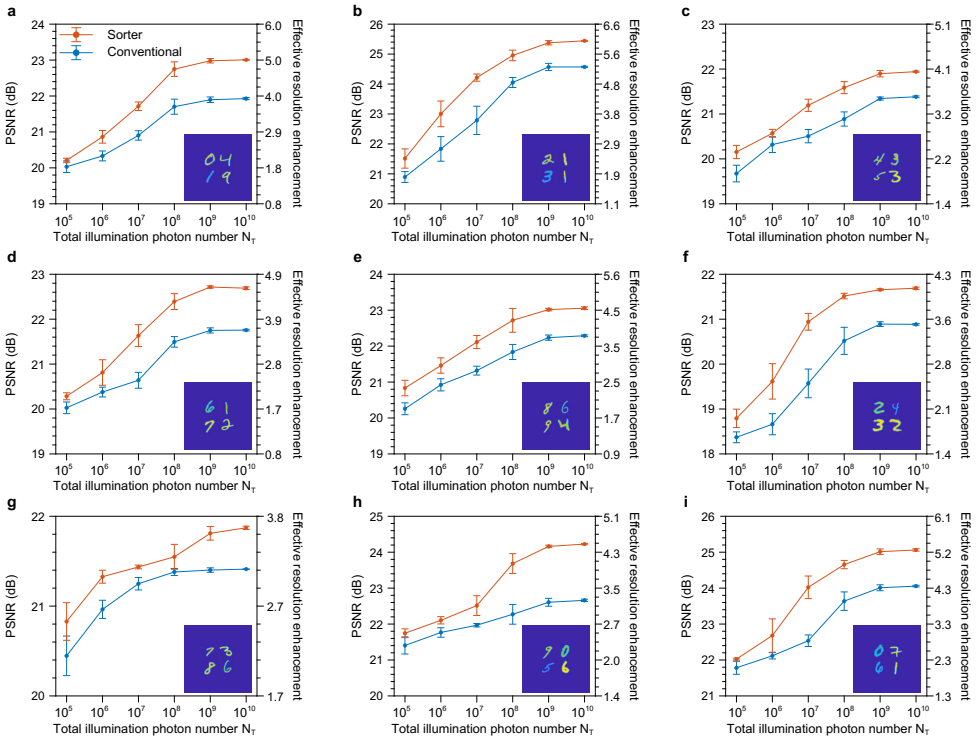

Fig. S3. (a-i) Performance characterization for nine different objects. The object image is shown as an inset in each figure.

REFERENCES

1. V. Centonze and J. B. Pawley, "Tutorial on practical confocal microscopy and use of the confocal test specimen," in *Handbook of biological confocal microscopy*, (Springer, 2006), pp. 627–649.
2. A. Janssen, "New analytic results for the Zernike circle polynomials from a basic result in the Nijboer-Zernike diffraction theory," J. Eur. Opt. Soc. **6** (2011).

3 Herriott Cell

3.1 A Brief Review of Quantum Imaging Experiments

This section will review some previous quantum imaging experiments to understand the need for an image-preserving delay line (IPDL). These experiments include, interaction-free measurements, ghost imaging, and alternative techniques that use both or neither of these first two techniques.

3.1.1 Interaction-Free

Interaction-free (IF) measurement [48] is the detection of the presence of an object without interacting with the object. This concept leads to IF imaging [49] where imaging is done with less than the classically expected amount of light being scattered or absorbed by the object. Elitzer and Vaidman (EV) presented an original scheme for interaction-free measurement. When this method is successful it can permit determination of the presence of an object without any light interacting with said object [50]. We can consider a shell thought experiment where there are two shells and under one of these shells lies a pebble. The pebble will disintegrate if it is touched by the light. The goal is to determine where the pebble is without destroying it. Clearly, if we simply lift a shell we will know where the pebble is, however, in half of the cases this will destroy the pebble. In contrast, with the shell thought experiment, the goal of interaction-free measurements would be to determine the presence of an object without any prior information. The EV scheme shown in **Figure 8** places the pebble or object in one arm of a Mach-Zehnder interferometer and has a single photon pass through.

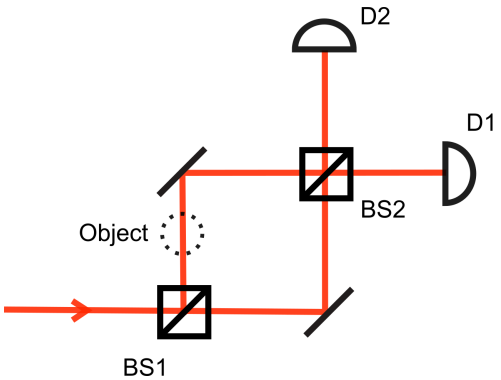

Figure 8: Elitzer and Vaidman scheme [50] for interaction-free measurement based on a Mach-Zehnder interferometer. The interferometer is balanced such that the interference leads to no counts at one detector and all counts arriving at the other. An object placed in one arm destroys the interference allowing counts at both detectors.

It is possible to balance the interferometer in such a way that the interference between the two arms

of light leads to no counts at one of the detectors and all of the counts at the other. However, if one were to put an object blocking one of the paths, this interference is destroyed leading to the possibility of counts at both detectors. In this scheme we have 3 possibilities of measurement that may occur. The first is interaction-free, the object is detected without absorbing the photon. This is indicated by a click at detector 2. This has a 25% probability of occurring. The second is interaction-full, the object is detected by absorption. This has a 50% probability of occurring. The third is no-result, detector 1 clicks and we cannot say if the object is present or not. This occurs with a 25% probability.

Kwait *et al.* [51] performed an experimental demonstration of the EV scheme for interaction-free measurement and were able to achieve the theoretically predicted 50% interaction-free result (i.e. when a measurement is made there are equal probabilities of it being interaction-free vs. interaction-full). The no measurement results are discarded. Using an alternative scheme that combines the quantum Zeno effect with the interaction-free measurement, they were able to achieve up to 70% interaction-free measurements.

This idea of interaction-free measurement was first extended by White *et al.* [49] to interaction-free imaging in 1998. They were able to measure the thicknesses of various wires, fibers, filaments, and human hair. Building on the previous work on interaction-free imaging, they used the experimental setup shown in **Figure 9** that was similar to the EV scheme. The use of polarizing beam splitters and half-wave plates is such that without the presence of the object, all counts will be found at one detector, say D_1. Following the insertion of the object, clicks at the other detector, say D_2, indicate that an interaction-free measurement has taken place. The proportion of D_2 clicks is dependent on the orientation of the half-wave plates.

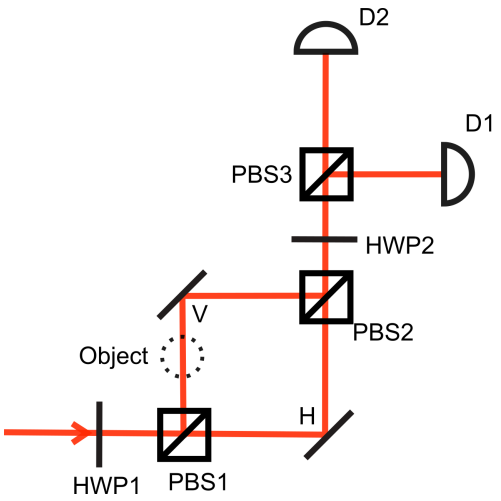

Figure 9: White's scheme [49] for interaction-free imaging. This scheme expands on the EV scheme, using half-wave plates (HWP) and polarizing beam splitters (PBS) to send H and V polarizations in separate arms in a Mach-Zehnder interferometer, forcing all clicks at D_1 unless proper orientation of the HWPs allows for interaction-free clicks to occur at D_2

Interaction-free imaging opens the possibility of imaging systems that would previously have been limited by a low power-induced optical damage threshold, e.g., biological samples or cold atom clouds, which would be destroyed by the photons in conventional imaging [49].

3.1.2 Ghost Imaging

In interaction-free imaging, there is no light interacting with the object. In ghost imaging, the light used to image the object never interacts with the object. However, there is still light that interacts with the object [52]. This is done using correlated light fields, one of which is imaged and the other that interacts with the object. These correlated light fields can be generated both classically [53] and in the quantum domain [54]. An example of this optical setup is shown in **Figure 10**.

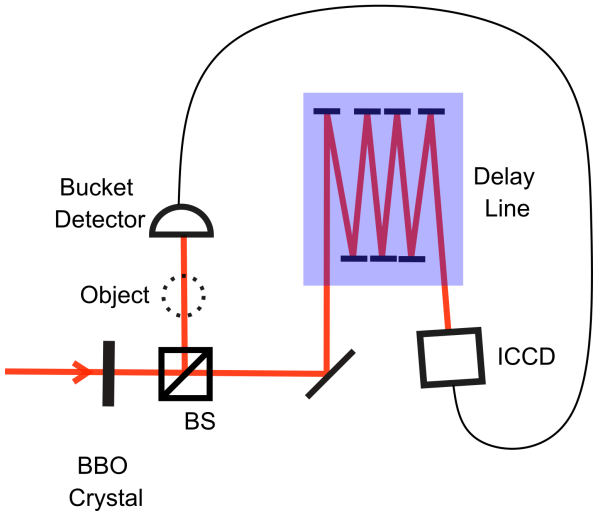

Figure 10: A general diagram illustrating the concept of ghost imaging. A nonlinear barium borate (BBO) crystal is pumped to create two photons through spontaneous parametric down-conversion. The first photon (idler) interacts with the object and is recorded by a bucket detector to trigger the connected intensified charge-coupled device (ICCD) camera. The second photon (signal) is held in an image-preserving delay line to account for the electrical delay between the bucket detector and the camera. Most importantly, the photon that is imaged is not the photon that interacts with the object.

The original ghost imaging experiment [54] was performed in a quantum setting using the correlation between signal and idler pairs produced through spontaneous parametric down-conversion (SPDC) by pumping a nonlinear crystal. An aperture placed in front of a detector (signal arm) is seen in the idler arm by scanning a fiber across the transverse plane and looking for coincidence counts. The image information is revealed through the correlations between the signal and idler photons. The coincidence counts are recorded and only the signal photons that are coincident with an idler will be recorded to reveal the image. More detailed information on the physics behind ghost imaging using correlated photons can be found in reference [55].The detection of the signal photon is triggered by the detection of the idler photon. Summing over the signal photons that are detected in coincidence with an idler reveals the image. Because of the timing of this triggering, there is a delay between the detection of the idler and the signal photons. During this time, the signal photons are stored in an image-preserving optical delay line.

Ghost imaging presents many new and exciting opportunities. One potential benefit of ghost imaging is the possibility to have non-degenerate signal and idler wavelengths. This would allow for a measurement to take place with one wavelength interacting with the object and another wavelength being used for detection. This is useful for cases where one might want to image at a wavelength where the detectors are not as efficient [55]. A huge advantage offered by ghost imaging is the high contrast images produced

due to gating the camera. The triggering allows for the background noise to be easily omitted [52]. One can also obtain images with very few photons (thus opening the possibility for imaging samples that are prone to damage). There are clearly many applications of ghost imaging in microscopy.

3.1.3 Alternative Techniques

Another interesting quantum imaging proposal is imaging with undetected photons [56]. In this method, the photons used to illuminate the object do not need to be detected, and coincidence detection is not required. Since coincidence detection is the main reason for requiring a delay line, this proposal is less relevant to the present Herriott cell project. However, it is still of interest in terms of quantum imaging techniques.

In 2019, the two techniques of interaction-free imaging and ghost imaging were combined to create interaction-free ghost imaging (**Figure 11**) [57]. In this approach, entangled photon pairs are generated using SPDC and one photon is sent to the interferometer to perform the interaction-free measurement, while the other photon is held in an image-preserving delay line. This latter photon is then imaged using an ICCD camera, which is triggered in coincidence. This combination of techniques allows for the photon illumination to be drastically reduced while maintaining the same quality as conventional ghost imaging. It is also sensitive to phase shifts and polarization changes so it could be used to image phase-only objects.

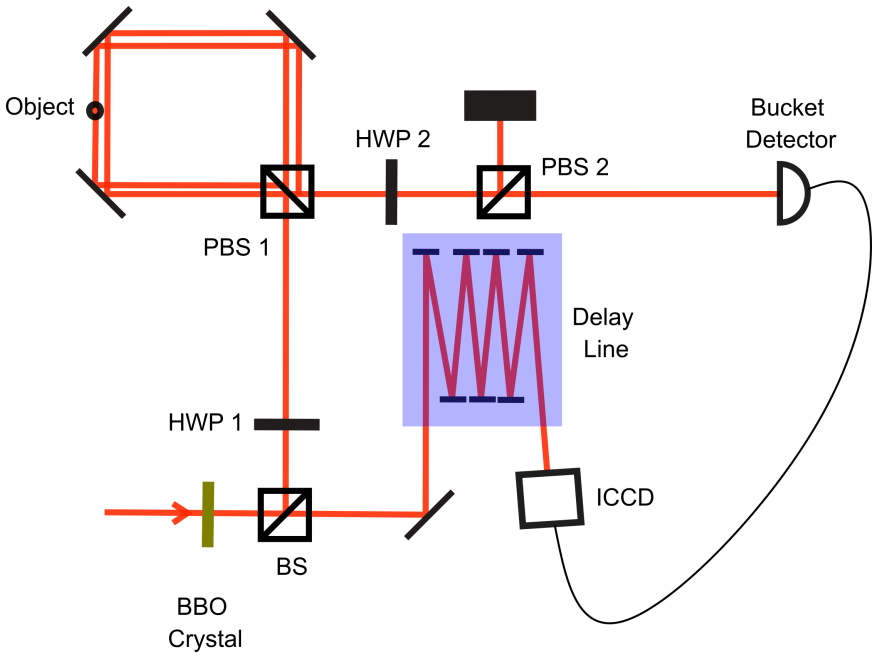

Figure 11: Interaction-free ghost imaging combines the interferometer of interaction-free measurement with the correlation of ghost imaging [57]. Note that once again there is the need for an image-preserving delay line.

To conclude, we will reiterate the need for an image-preserving delay line (IPDL). In ghost imaging with entangled photons, the herald triggers the sensor and the signal interacts with the system. These photons are detected in coincidence. There is a delay between the trigger and the sensing, during which time the signal photon must be stored, hence the need for an IPDL.

3.2 Motivation: Herriott Cell as an Image-Preserving Delay Line

The need for an IPDL was described in the review of various quantum imaging experiments given in the previous section. The most common implementation for an IPDL is a series of planar mirrors with lenses in between. This is essentially a sequence of 4f systems that repeatedly re-image the light field. Given the speed of light, a delay of 30 ns (as required for a typical triggering system) would have the light travel 9 m. Thus, a typical 4f IPDL would occupy a significant amount of space on an optical table. Another device that is capable of storing light for a fixed duration is a Herriott cell (HC). In 1963, Donald R. Herriott created a high-Q, multi-pass spherical-mirror interferometer [58]. He intended it to be used for spectral measurements of lasers by having one mirror oscillate to scan the wavelength. The following year, Herriott described the trajectory of the beam within this interferometer [59]. Of note, an off-axis ray of light creates a path that lies on the surface of a hyperboloid, most commonly resulting in an ellipse. Through the repeated reflections, rays can retrace their paths and create resonances. The intended use was to create a long effective path length in an active medium, contained in a small shell

for use in laser amplifiers. Today, Herriott cells are used in a similar fashion but for multipass absorption spectroscopy. Finally, in 1965 it was Herriott who proposed that the cell be used as a dispersionless optical delay line for use in filtering or storage of information [60]. This cell is shown in **Figure 12**. With this cell, Herriott was able to achieve over 1000 reflections between two spherical mirrors.

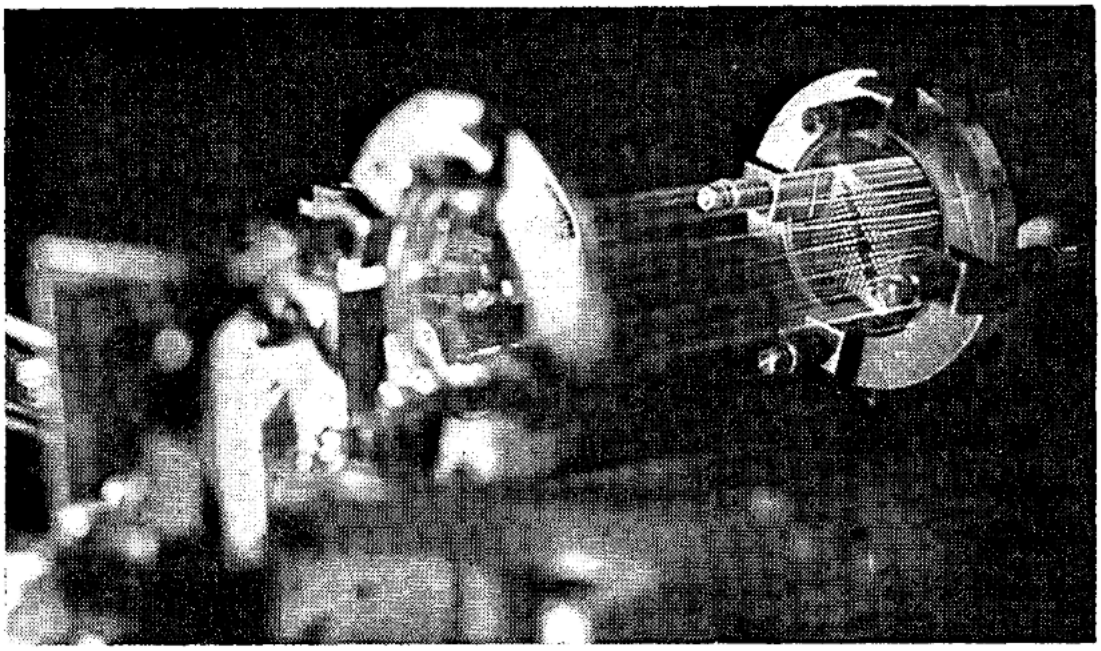

Figure 12: The original Herriott cell filled with smoke to make the beam visible, reprinted with permission from [https://doi.org/10.1364/AO.4.000883] [60] © The Optical Society.

In short, this device is essentially a modified Fabry-Perot (two mirror) cavity, composed of two spherical mirrors with a small hole drilled into one (or both) of the end mirrors. Light is launched through the hole and is reflected repeatedly, before re-emerging. However, in contrast to the standard Fabry-Perot cavity, the HC is frequency insensitive due to the hole preventing interference between the different reflections in the cell. This frequency insensitive quasi-cavity offers the possibility of an IPDL in a compact setup.

A spherical mirror can be seen as the combination of a planar mirror and a lens. In this way, the HC can also be understood as a series of approximate 4f imaging systems just like a typical IPDL. However, due to the nature of the reflections and the shape of the cell, it will be more compact. This size reduction is advantageous and has numerous applications, e.g., portable systems or systems requiring multiple independent delay lines. There also exists the potential for miniaturization since there are only two components to the HC. Furthermore, the HC allows for significant variations in delay times with a small adjustment in the distance between the cell mirrors without the need for significant additional re-alignment. More details will be given in Section 3.6 on the characterization of the HC.

While we intend to characterize the HC for its use as an IPDL, the HC is not an unknown device in the world of optics. The HC is commonly used in absorption spectroscopy. Its long path length and compact design make it particularly well suited for this task. There are commercially available HCs (e.g. through ThorLabs, Inc., St. Laurent, QC) that offer a 10.5-m or 31.2-m optical path length in a cell that is only 0.4-m long. These cells are built into a chamber that can be filled with different gases for multipass absorption spectroscopy. Interestingly, a multi-channel HC configuration was designed for this purpose on the 2009 Mars Science Laboratory mission. This multi-channel nature is enabled by having multiple lasers that pass through multiple input and output ports to the HC. The spectroscope was used to help measure gas abundances in the atmosphere of Mars as a part of the Sample Analysis at Mars (SAM) Instrument Suite. [61].

3.3 Intuition Behind Using the Herriott Cell as an IPDL

As previously described, an image-preserving delay line is commonly comprised of a series of 4f systems. Using a ray transfer (also known as ABCD) matrix analysis (**Figure 13**) we can determine how a traditional IPDL affects a light beam and adjust our Herriott cell, potentially through the addition of an extra lens on the output, to match the traditional 4f approach. This ray-tracing method is based on an input and output plane on either side of an optical system.

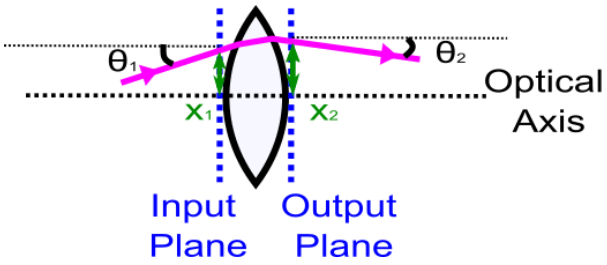

Figure 13: Illustration of the system for ray-tracing or the ABCD matrix method, which is used to relate the ray angle and height at the input plane before an optical element to the angle and height output plane after the optical element.

$$\begin{pmatrix} x_2 \\ \theta_2 \end{pmatrix} = \begin{pmatrix} A & B \\ C & D \end{pmatrix} \begin{pmatrix} x_1 \\ \theta_1 \end{pmatrix}. \tag{6}$$

The ABCD matrix shown in **Equation 6** is used to relate the incoming beam's distance from the optical axis and angle, to the outgoing beam's angle and the distance from the optical axis (**Figure 13**). Different optical systems will have different representative matrices. For our calculations we will require

the following matrices [62]:

Free-space propagation for a distance d

$$\begin{pmatrix} 1 & d \\ 0 & 1 \end{pmatrix} \tag{7}$$

Thin lens with a focal length f

$$\begin{pmatrix} 1 & 0 \\ -1/f & 1 \end{pmatrix} \tag{8}$$

Spherical mirror with an effective radius of curvature of R_e

$$\begin{pmatrix} 1 & 0 \\ -2/R_e & 1 \end{pmatrix} \tag{9}$$

The effective radius of curvature for a horizontal (x) beam coordinate

$$R_e = Rcos(\theta). \tag{10}$$

The effective radius of curvature for a vertical (y) beam coordinate

$$R_e = \frac{R}{cos(\theta)}. \tag{11}$$

First, the traditional IPDL is a series of 4f systems as shown in **Figure 14**. A single 4f system consists of free space propagation for the distance of the focal length of the first lens, f_1, then the first lens, then free space propagation for the sum of the focal lengths $f_1 + f_2$, followed by the second lens, and finally free space propagation for the focal length of the second lens. This has the net effect of magnifying the image by the factor $M = -\frac{f_2}{f_1}$. The series of 4f systems allows for the image to be preserved over a long distance by repeatedly re-imaging. For simplicity, we can consider a single 4f system in our calculation and understand that the repetition would be equivalent to the repeated multiplication of this matrix, which we can see is equivalent to magnifying by the ratio of the focal lengths, as previously described.

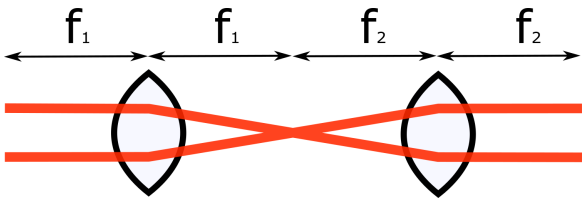

Figure 14: Traditional 4f system

$$M = \begin{pmatrix} 1 & f_2 \\ 0 & 1 \end{pmatrix} \begin{pmatrix} 1 & 0 \\ -1/f_2 & 1 \end{pmatrix} \begin{pmatrix} 1 & f_2 \\ 0 & 1 \end{pmatrix} \begin{pmatrix} 1 & f_1 \\ 0 & 1 \end{pmatrix} \begin{pmatrix} 1 & 0 \\ -1/f_1 & 1 \end{pmatrix} \begin{pmatrix} 1 & f_1 \\ 0 & 1 \end{pmatrix}, \tag{12}$$

$$M = \begin{pmatrix} -f2/f1 & 0 \\ 0 & -f1/f2 \end{pmatrix}. \tag{13}$$

Second, we have the Herriott cell with a single hole. In this scenario, the beam enters and exits through the same hole (**Figure 15a**) and we might consider it as though the beam has reflected off of the back surface of the mirror (**Figure 15b**). Since we want to use the cell as an IPDL, we must identify which components will allow us to use the cell in this manner, leaving our image unchanged (i.e., a 4f system with equal focal lengths). This is done by setting the product of the unidentified component and the HC matrix equal to the identity matrix in **Equation 14**.

(a) Single hole Herriott cell

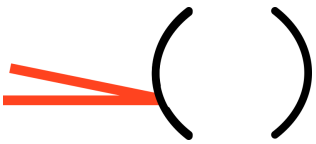

(b) Rebound

Figure 15: Intuition for the behaviour of a single entrance and exit hole Herriott cell

As the HC operates in a regime where $\theta << 1$, the small angle approximation gives $cos(\theta) \approx 1$ which leads to $R_e = R$.

$$\begin{pmatrix} A & B \\ C & D \end{pmatrix} \begin{pmatrix} 1 & 0 \\ -2/R & 1 \end{pmatrix} = \begin{pmatrix} 1 & 0 \\ 0 & 1 \end{pmatrix}, \tag{14}$$

$$\begin{pmatrix} A & B \\ C & D \end{pmatrix} = \begin{pmatrix} 1 & 0 \\ 0 & 1 \end{pmatrix} \begin{pmatrix} 1 & 0 \\ 2/R & 1 \end{pmatrix} = \begin{pmatrix} 1 & 0 \\ 2/R & 1 \end{pmatrix}, \tag{15}$$

$$\begin{pmatrix} 1 & 0 \\ -1/f & 1 \end{pmatrix} = \begin{pmatrix} 1 & 0 \\ 2/R & 1 \end{pmatrix}, \tag{16}$$

$$-\frac{1}{f} = \frac{2}{R}, \tag{17}$$

$$f = -\frac{R}{2}. \tag{18}$$

Multiplying by the right inverse of the spherical mirror matrix, we can solve for the unidentified component in **Equation 15**. We notice that this result has a similar form to the ABCD matrix for a thin lens (**Equation 16**). Equating the bottom left matrix components (**Equation 17**) gives the result (**Equation 18**). For a concave mirror, R is positive, which yields a negative focal length. Hence, we could place a diverging lens after the Herriott cell to complete our 4f system.

Third, we have the Herriott cell with a two holes as shown in **Figure 16**. Properly aligned, the beam enters through one end of the cell and exits at the other. This scenario may be considered as though the beam has simply passed through free space the length (d) of the cell, assuming that the transverse movement of the beam is negligible compared to the separation between the two mirrors. In this case, we would need to place a lens on either side of the "free-space" of the cell to create the 4f imaging setup. We can then solve for what lenses would be appropriate. Mathematically, this is shown in **Equation 19**.

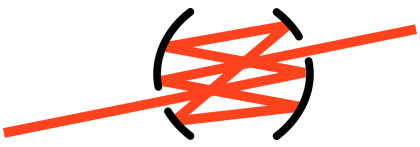

Figure 16: Herriott cell with entrance and exit holes on opposite mirrors

$$\begin{pmatrix} 1 & 0 \\ 0 & 1 \end{pmatrix} = \begin{pmatrix} 1 & f_2 \\ 0 & 1 \end{pmatrix} \begin{pmatrix} 1 & d \\ 0 & 1 \end{pmatrix} \begin{pmatrix} 1 & f_1 \\ 0 & 1 \end{pmatrix} = \begin{pmatrix} 1 & f_1 + f_2 + d \\ 0 & 1 \end{pmatrix}, \tag{19}$$

Solving for d yields **Equation 20**,

$$f_1 + f_2 = -d. \tag{20}$$

where the focal lengths of lenses would need to add to the negative of the distance between the two mirrors.

These simple model calculations represent the intuition behind the Herriott cell and an attempt to understand how it functions. A more in-depth simulation of the ray transfer matrix that will follow the light through the cell is presented in the following section.

3.4 Herriott Cell Simulations

The ABCD matrix approach can be extended to consider multiple reflections tracing the path the beam takes as it travels through the cell. We wrote a MatLab code to perform these matrix multiplications and beam-tracing calculations. A short description will be included here with the emphasis being placed on the results and the understanding gained from the simulations.

The beam path is followed from initial transverse angles and input position at the centre of the hole, through its trajectory in the cell, counting the reflections on both mirrors and tracking their locations, until it exits at a recorded angle and output position. Because the beam is followed closely, the free space distances between mirrors (tracking the total delay time) is altered to account for the transverse movement of the beam and the curvature of the mirrors. This allows for a more accurate depiction of the light path.

The following parameters are adjustable: input angles; input position in (x,y) coordinates; and the mirror separation. The goal of the simulation was to determine how these parameters affect the Herriott cell performance in terms of delay time, efficiency, and mode dependence.

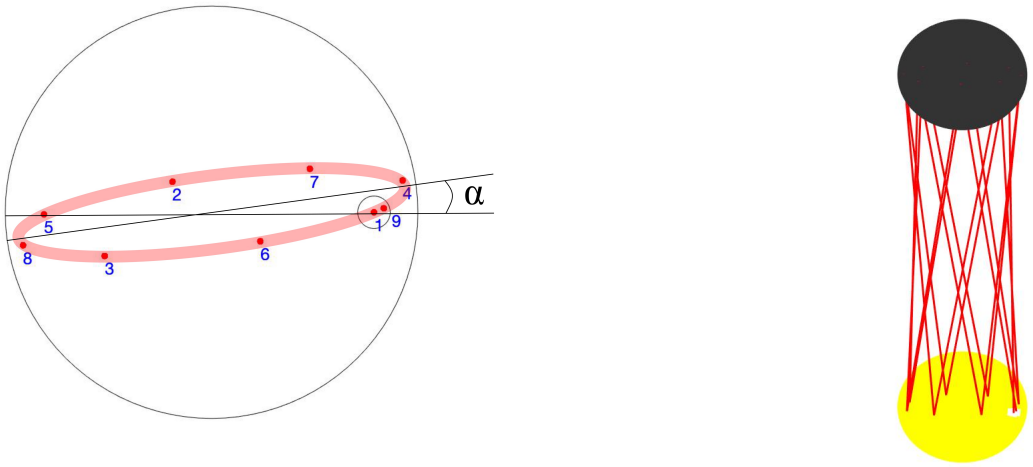

(a) Reflection locations on the gold mirror, the mirror with the entrance and exit hole of the HC.

(b) Full beam trajectory through the HC.

Figure 17: The beam path through the cell can be calculated using ABCD matrices, allowing us to track the position of the beam at any point during its stay in the Herriott cell.

Figure 17 shows an example to offer some insight into how the cell works. This is calculated using a series of ABCD matrices as previously described. We can see that in **Figure 17b** the beam forms a cylindrical shape that narrows at the centre of two mirrors. More interesting to note is the shape that can be seen on the end mirrors. The reflections form an elliptical path which is determined by the input angle (θ in the ABCD matrix calculations). The larger the angular deviation from 0, in either direction, the wider the ellipse will be in that same direction. For a 0 rad x angle, a negative y-angle tilts the ellipse by an angle α as seen in **Figure 17a** while a positive y-angle tilts it opposite to this. The shape is formed in families of reflections, for example, it will take 5 reflections to make an ellipse. Since the final reflection does not exit through the hole, another round will occur and this process will continue until the beam escapes through the hole.

The overall cross-sectional area of the HC is, in theory, limited by the shape on either end and the area of this ellipse or arbitrary shape. Therefore, it would be desirable to maximize the number of reflections per unit area if we are looking to minimize the system size. In an early paper by Herriott and Schulte [60], similar elliptical shapes were presented; however, these authors also observed different Lissajous patterns as shown in **Figure 18** when slightly astigmatic mirrors were employed, as opposed to the traditional spherical mirrors.

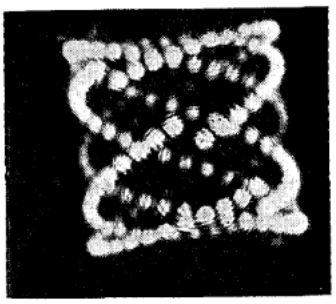

Figure 18: Nonsychronously sampled Lissajous patterns generated using astigmatic mirrors, reprinted with permission from [https://doi.org/10.1364/AO.4.000883] [60] © The Optical Society.

Another technique used to alter the beam trajectory was an additional small mirror to deflect the beam from its original path. This perturbing mirror would put the beam onto a different elliptical path. One might consider having two sets of ellipses, one of which does not connect with the hole and one of which does, as shown in **Figure 19**.

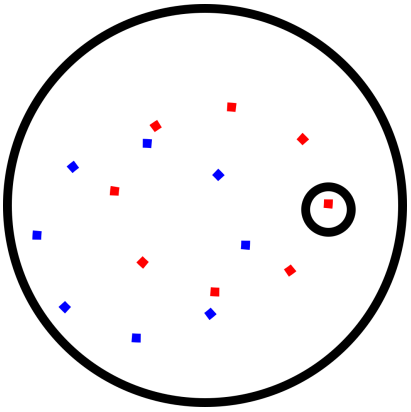

Figure 19: The HC could, in theory, have multiple ellipse patterns where only one of them interacts with the hole. By switching between the patterns, it would be possible to choose when the light exits the hole, storing it indefinitely.

Using a small mirror that could be inserted or removed to shift the light between these two ellipses would allow for light to enter the cell and then be held in the exit-free ellipse until we wish for it to exit. However, in practice, the particular placement of a small optical element without interfering with the rest of the beam trajectory proved to be too difficult to accomplish during the scope of this project.

As mentioned earlier, the HC is essentially a modified Fabry-Perot cavity. However, the presence of the hole destroys the interference and allows it to be wavelength independent. We might still expect there to be quasi-resonances, or cell lengths offering long delays. To explore this, the input parameters (input angles; input position in (x,y) coordinates) were held constant and the cell length was varied to determine

the number of reflections that were occurring at each cell length. Twice the cell length multiplied by the number of reflections on the mirror opposite the hole (in our case this is a silver mirror) gave the total delay for the cell, without accounting for the small differences due to the transverse movement of the beam. **Figure 20** provides an example of this effect. Understanding the relationship between the delay and the alignment of the cell would allow us to build an HC with specific characteristics that we desired.

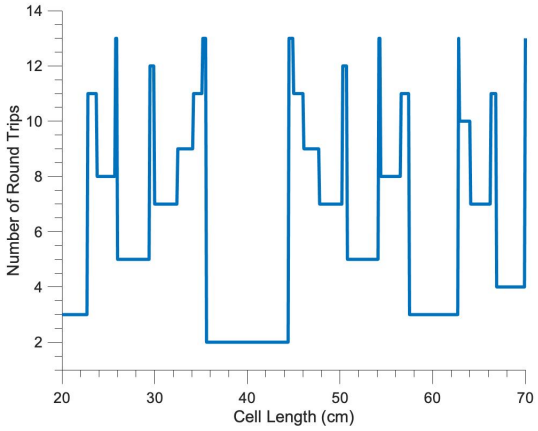

(a) Varying the mirror separation or cell length results in different numbers of round trips through the HC

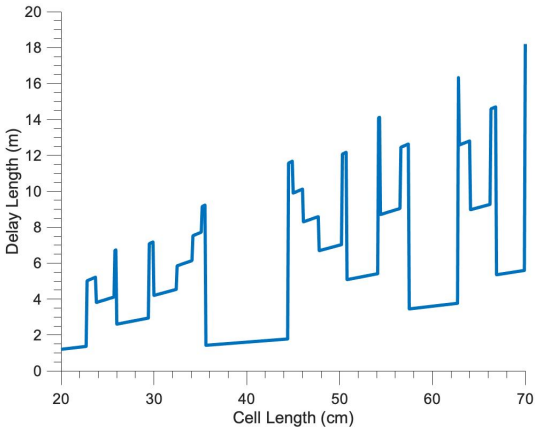

(b) The cell length is associated with different delay lengths

Figure 20: A sample fixed input angle with a varied cell length is used to assess the impact on the number of round trips and therefore delay.

In our experimental setup, the mirrors have a 40-cm radius of curvature. A cavity with these mirrors would be stable up to lengths of 80 cm [63]. However, they are often most stable for lengths smaller than the radius of curvature. In practice, we were able to use lengths up to 40 cm without significant rearrangement of the optical table. Therefore, we decided to simulate in more detail and the results are shown in **Figure 21**, leading to several notable findings. First, there are plateaus, regions where the reflection number is the same for a range of cell lengths. This is ideal since it makes alignment easier and more robust. Second, the plateaus appear in families, e.g., starting at 20 cm one can trace a smooth curve through the lower plateaus. Third, there are regions where multiple plateaus with varying reflection numbers are quite close together. Recall, we are interested in creating a delay line that can achieve variable delays without significant realignment. The proximity of multiple plateaus allows us to switch between them using a precise translation stage. This also offers the possibility of automating the stage and therefore automating movement between variable delay times in the cell.

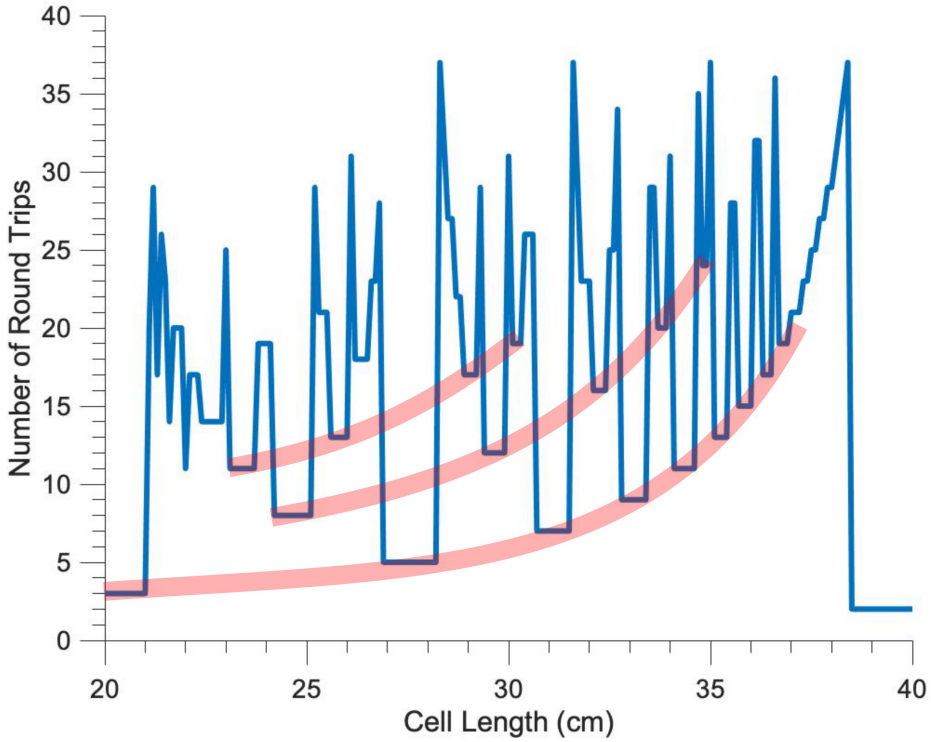

Figure 21: For a fixed input angle, there are plateaus where for a range of cell lengths the number of round trips is constant. Varying the cell length offers many different plateaus each with different numbers of round trips. The plateaus can be grouped into families (in red) and many different plateaus can be accessible within a small range of cell lengths.

A delay line with no light at the end would be completely useless. It is important to us to maintain high efficiency throughout this delay process. The HC is a simple structure consisting of two mirrors and free space. Theoretically, dielectric mirrors with efficiencies greater than 99.999% [64] could be used which would allow for 1000 reflections at a 1% drop in power. However, this high efficiency comes at a trade-off with the bandwidth. Fortunately, due to the presence of the hole, the HC intrinsically has unlimited bandwidth, so any power decrease would be due to the mirrors. Ignoring the efficiencies of the mirrors, we tuned other parameters to determine the optimal configurations for maximum efficiency. In the simulation, the efficiency is determined by how much of the mode leaks off of the mirror, i.e., a reflection fully contained on the mirror would have an efficiency of 100% and a reflection off the mirror would have an efficiency of 0%. Similarly, when the beam is exiting, the efficiency calculation is reversed so that 100% efficiency is a reflection fully contained in the hole.

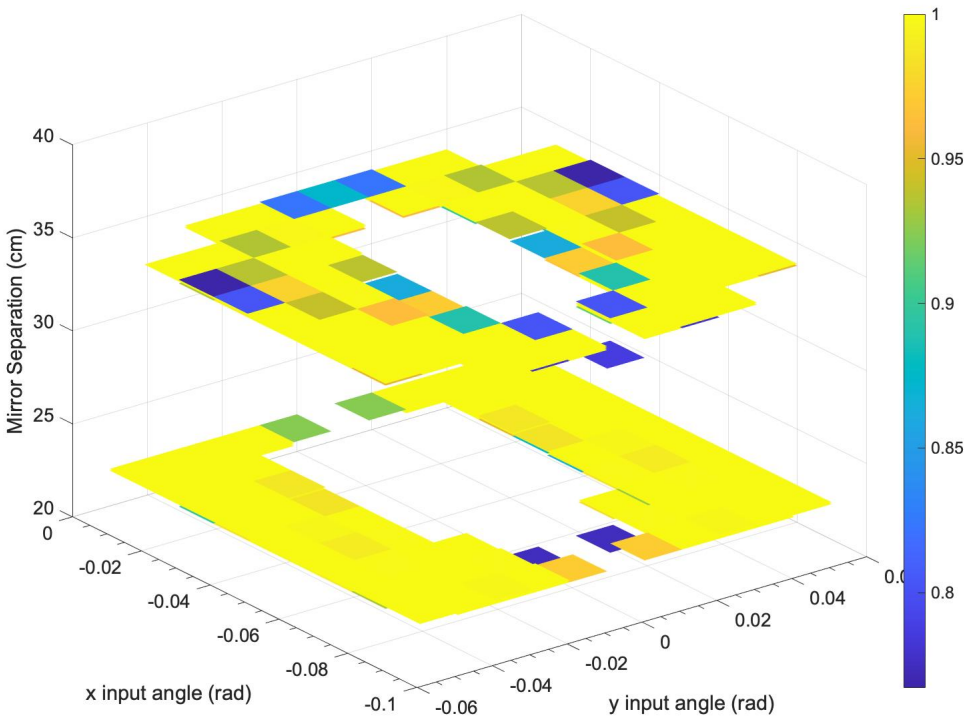

Figure 22: Efficiencies for 20 round trip cell configurations. Note that the 20 round trip configurations take place at two lengths of 22 cm and 34 cm with each length having their own ring of acceptable input angles in order to have an efficiency >75%

As shown in **Figure 22** for the example of a 20 round trip cell, we can calculate the efficiency for any potential lengths and input angles. Since there are quite a few parameters to consider, it is intuitive to settle on the desired delay and cell length, or range of acceptable lengths, and then find the appropriate input angle. In this case, we have two possible lengths that will yield 20 round trips. If we choose the 34 cm long cell for a longer delay, we can then opt for an input angle that will give us the highest possible efficiency.

Another factor to consider is how efficient the HC will be for image preservation. Any image can be decomposed into a basis of HG modes. If many of these modes are preserved inside the cell, then there will be good image preservation. Until this point, we have been working with HG00. As the mode index increases so does the mode size, leading to a decrease in efficiency. To have an image-preserving delay line, it would be necessary to preserve these larger order modes and not simply HG00. We used the same code to test the efficiencies of higher-order modes. Generally, a decrease in efficiency due to increased mode size will only occur if the reflections on the mirror tend to fall close to the edge.

3.5 Characterization Methods

3.5.1 Off-Axis Holography

To understand the technique used to recover the modes in our setup, a brief introduction to holography is provided here followed by its application to the technique of off-axis holography. For readers who are more interested in the mathematical details behind holography please refer to reference [63] for further information.

An arbitrary monochromatic field, i.e., 3 dimensions E(+)(x,y,z) can be completely determined by a 2-dimensional slice, e.g., E(+)(x,y,0). This is because we can take this slice and propagate it to determine the field at any other point. A hologram is a device that takes advantage of this principle. The hologram is a thin (ideally 2D) optical element with a complex transmission that is proportional to the electric field of the 2D slice. Thus, this hologram can be used to generate whole 3D images.

The question is then, how is a hologram constructed? Hologram construction requires both the intensity and the phase to be encoded into the slice so that as previously described, said slice determines the electric field at any point in space. This encoding is accomplished by using an interference measurement. As shown in **Figure 23a** reference wave and the object wave are incident onto the film (to become the holograph). The film records the intensity of this reference and object wave mixture and the superposition of the two waves causes the phase to also be encoded into the image. To retrieve the information from the hologram, the same reference beam is shone on the developed hologram **Figure 23b**. However, this will result in a forward propagating reference wave as well as the reconstructed wave and its conjugate wave (not shown in the figure). Separating the waves can be achieved by ensuring that the angle between the reference wave and object wave is large enough.

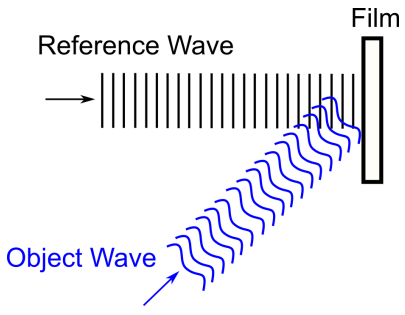

(a) The incoming reference wave and object wave interfere at the film

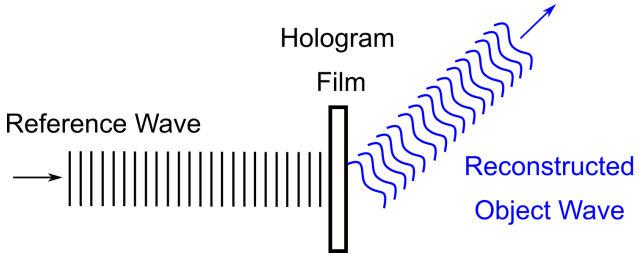

(b) Shining a reference wave on the developed hologram film returns the reconstructed object wave

Figure 23: A hologram is created using interference between the object and reference beams. This same reference wave is used to retrieve the reconstructed object wave from a developed hologram.

This angular separation leads to the concept of off-axis holography. To create the hologram, the laser beam is split into a reference wave and a wave that will interact with the object. The resulting interference between these waves is then captured on the film. This is identical to the procedure that we use in measuring the fidelity of our HC, where the HC will be the object to be recorded and we will image the interference between the beam held in the cell and a reference beam. This principle of holography is directly applied for spatial light modulators, which, as described next, use holograms to shape light as desired.

3.5.2 Mode Generation

The following section discusses the use of spatial light modulators (SLM) in mode generation. Since the SLM was employed as a tool in this experiment and not a main focus of the overall approach, the description will be concise and only to describe the use of the SLM in our experiment. We will focus less on the mathematical derivations and more on the application. For more information on SLMs please refer to reference [65].

An SLM is a device that can control the phase, amplitude and polarization of light [65]. For our case, we use an SLM that operates in a reflective mode such that the light reflects off of the SLM and returns in our desired state. Transmissive SLMs wherein the light is altered upon transmission through the SLM also exist. An SLM is essentially a second computer monitor that displays a hologram. This hologram acts to manipulate liquid crystals (LC) to control the light in the desired manner. Finding the appropriate hologram to produce the output is therefore a key step in the process. We produce our hologram using a MatLab program [66] that generates the complex electric field for HG modes, which gives us both the phase and amplitude information required to generate the hologram. Our final hologram displayed is a combination of this field with a binary grating.

Recall that this project focuses on the preservation of the modes rather than their initial generation. The SLM and codes we used served to produce modes of an adequate quality. Better SLMs are certainly commercially available albeit at a higher cost. We optimize the positioning of the hologram on the SLM to maximize the intensity of our desired beam as well as perform minor aberration corrections to achieve a good quality HG mode. The diffracted light that is in the desired pattern will end up on-axis with the undiffracted (i.e., unchanged) light in the zeroth-order of diffraction. To avoid interference between these components, a grating is added to the hologram, which serves to shift the desired component away from the undiffracted light. There are multiple types of gratings as shown in **Figure 24**, the simplest

being the binary grating (used in our mode generation) which sends around 40% of the power into the first diffraction order [65]. In our code, we use a binary grating. Improving upon this, blazed gratings use a phase ramp and can send 100% of the power into the desired order [65].

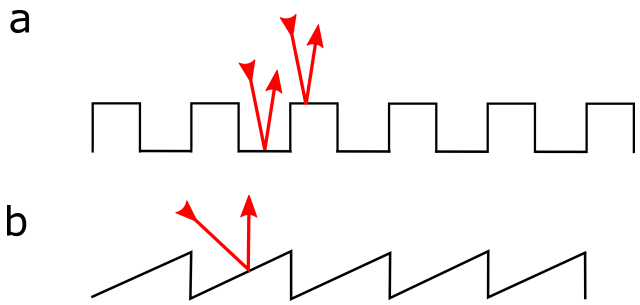

Figure 24: Two examples of diffraction grating types (a) binary grating, either on (white) or off (black) (b) blazed grating, ramps from off (black) through the greyscale until on (white) and then drops again

In order to select the desired order and block the unwanted orders, it is common to image the SLM using a 4f system. In this case, an aperture is placed at the focus between the lenses allowing only the desired order to pass. This is the technique used in our setup since we image the SLM onto the HC with the aperture placed appropriately.

3.5.3 Mode Reconstruction

We image the interference between the reference beam and the beam that passes through the HC using a CCD camera. We then analyze these data using MatLab by first reconstructing the mode and then computing the fidelity.

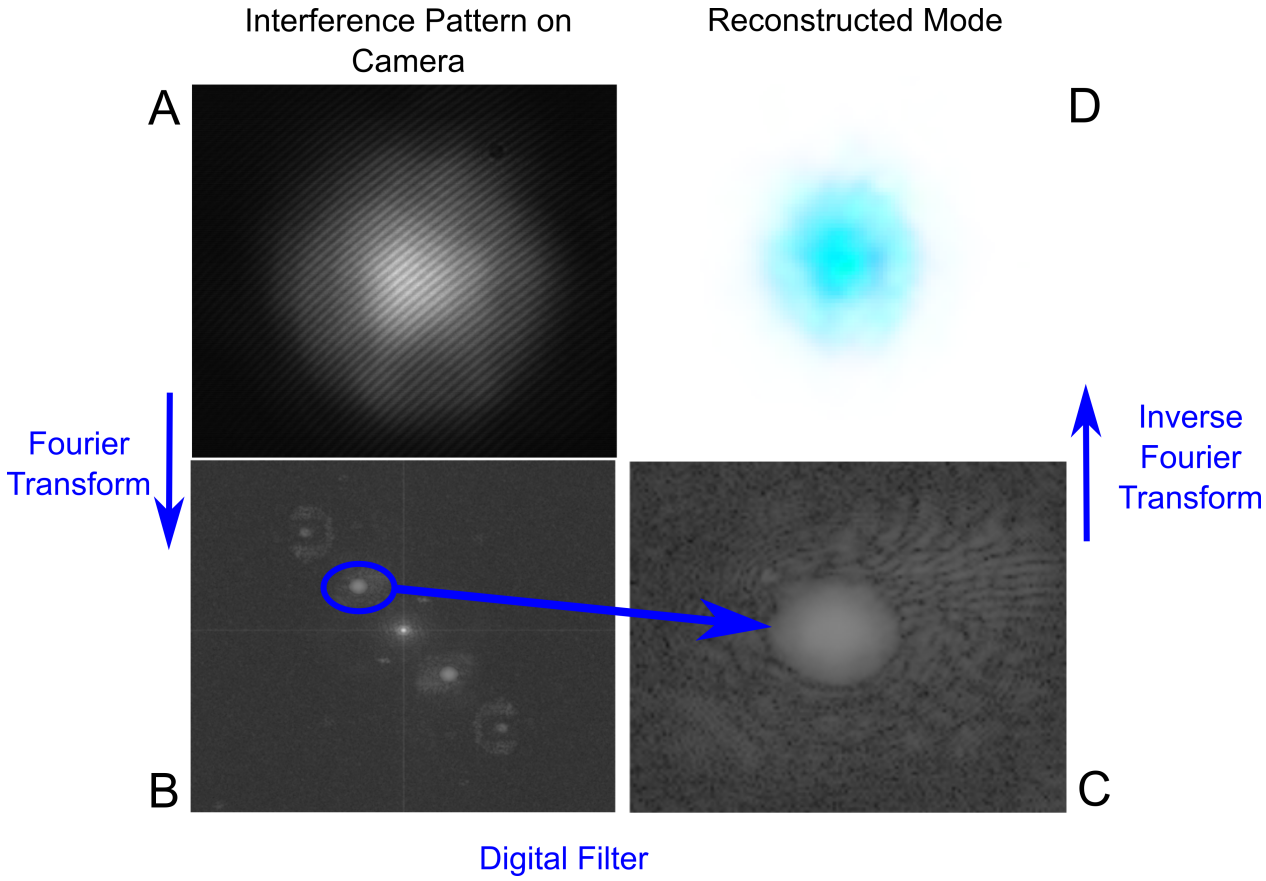

Figure 25: Mode reconstruction. First, the interference pattern recorded on the camera (A) After applying a Fourier transform (B) and a digital filter to select the mode of interest, image (C) is obtained. Once the mode is selected, an inverse Fourier transform returns our reconstructed mode (D).

The steps for mode reconstruction are shown in **Figure 25**. The first step is to take the Fourier transform so that we can work in the frequency domain. A digital filter is then applied to isolate the interference fringes that we are looking for. As visual inspection reveals, it is quite clear where the mode is and what is noise or other interference fringes generated by stray reflections. Once the region of interest is narrowed down, the filter is added to the Fourier transformed image. Since all that remains is the mode, a simple inverse Fourier transform returns the mode that was present in the HC arm without the interference from the reference beam.

Because we have both the phase and the intensity from the beam, we can propagate digitally to the desired (image) plane. While the HG modes are spatially invariant (so this was not needed for those reconstructions), to view an image after the HC one would need to place the camera in the image plane. Because of the crowded nature of our setup, putting a 4f system between the HC and the camera was not physically feasible. Instead, we digitally propagate the field to the desired image plane and analyze the images there.

3.6 Experimental Characterization of the Herriott Cell: Methods and Results

3.6.1 Setup

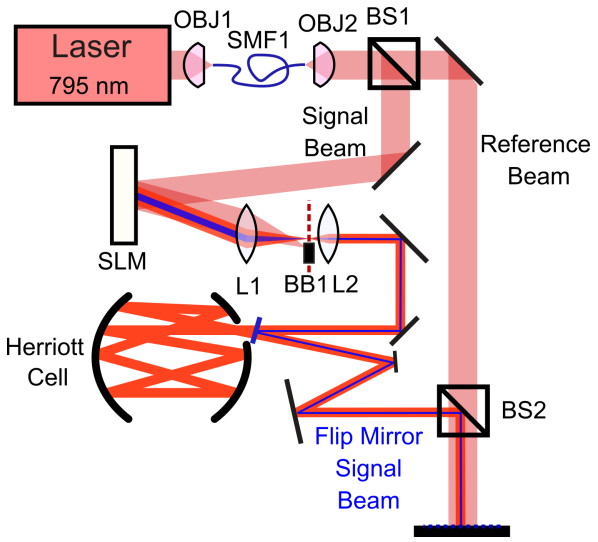

Figure 26: Experimental setup for characterization of the Herriott cell using off-axis holography

The experimental setup, illustrated in **Figure 26**, consists of an interferometer with a HC in one arm to measure the effect of the HC on the quality of the beam that passes through it, could be measured.

The diode laser is the Toptica DL Pro (TOPTICA, Inc., Farmington, NY, USA), with a wavelength of 795 nm. The light is focused (OBJ 1) into a single-mode fibre (SMF1) whose main purpose is to transport the beam from the laser to our experimental setup. The fibre also serves to clean the mode. This fibre is coupled to a polarizer, which allows for alteration of the polarization of the beam that will exit from the fibre. After exiting the polarizer fibre, the second objective lens (OBJ 2, f = 10 cm) collimates the beam to a large diameter slightly less than an inch. This allows the beam to pass through the 1-inch optics while affording large coverage from the reference beam on the camera and, more importantly, a large beam to take advantage of the full SLM. The beam then passes through a polarizing beam splitter (not pictured, between OBJ2 and BS1), which polarizes the beam by transmitting the p-polarized light and reflecting the s-polarized light which can then be blocked. This PBS is being used as a polarizer and has the added benefit of reducing the intensity of light in the overall system.

The first beam splitter (BS1) transmits light towards the SLM and the reflected beam is the reference

beam for the off-axis holography. The SLM (Cambridge Correlators) generates a chosen mode in the first diffracted order as described in Section 3.5.2. The first lens (L1, f = 50 cm) focuses the light from the SLM. Since the different diffraction orders occur at different angles, they will be focused to different spatial points. This spatial separation in the focal plane allows for the selection of the desired order by blocking the other orders using an iris (BB1). The second lens (L2, f = 20 cm) collimates the light as it passes into the HC. These two lenses (L1, L2) form a 4f system between the SLM and the entrance hole of the HC and reduce the size of the beam by a factor of 2.5. The beam should be large at the SLM to make use of the whole surface, whereas, at the HC the beam should be small to avoid clipping at the hole. The beam then passes through the HC or reflects off the optional flip mirror to simulate the case without the HC. The number of reflections is variable and was studied by changing the length of the cell. To this end, the silver mirror (Thorlabs CM254-200-P01) in the HC was placed on a translation stage. This allowed for precise movement of the mirror and altering of the cell length with precision through a range of roughly 5 cm. A gold-coated spherical mirror (Thorlabs CM508-200EH4-M02) with the entrance (and also exit) hole was fixed to the optical table. Both mirrors have a 40 cm radius of curvature.

Since, the entering and exiting beams are quite close to each other, a D-mirror is used to select the exiting beam and send it to recombine with the reference beam at the second beam splitter (BS2). The resulting interference is then recorded using a camera (Thorlabs DCC1645C). Note that the camera is not in the image or focal plane. Because HG modes are being used and they are invariant with spatial propagation, the fidelity of the mode can be assessed regardless of in which plane we image. For other images, we used post-processing to digitally propagate the field to the image plane and to assess the corresponding image.

3.6.2 Visible Reflection Numbers

Theoretical predictions from the simulations revealed that altering the length of the cell for a given input angle creates different plateaus with a different number of round trips. To experimentally validate these predictions, a red visible (650 nm) laser was used instead of the 795 nm laser. This permitted observation of the reflections on the gold mirror as shown in **Figure 27**.

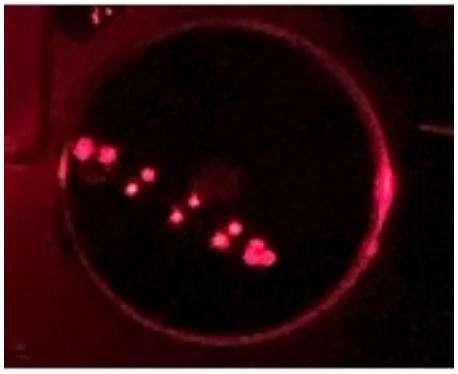

Figure 27: Visible reflections on the gold mirror for a 35.7-cm separation

The reflections from the gold mirror were counted as the cell was lengthened from 33.5 cm to 35.5 cm. The original mirror separation was measured using a tape measure between the two mirrors and then the silver mirror was moved using a translation stage. There was a much larger uncertainty in our original length measurement than in the length-changing measurements. For a reflection number to be valid at a given distance, the image of the HG00 mode out from the HC must be whole and not clipped. Using these criteria, the number of reflections and therefore round trips were counted as illustrated in **Figure 28**

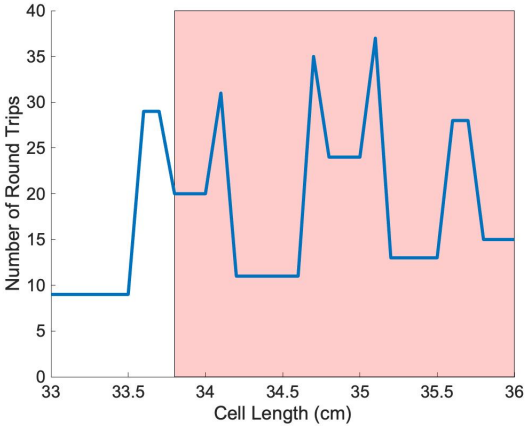

(a) ABCD matrix simulation of the number of round trips for an input angle of 0.009 rad in the x direction and 0.011 rad in the y direction

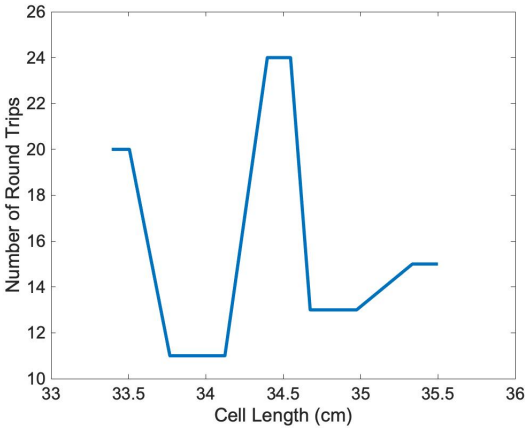

(b) Number of round trips calculated by counting the visible reflections on the gold mirror

Figure 28: A comparison between the simulated reflection numbers and the experimental values. Note here that the red zone in (a) corresponds well with (b)

The input angle of the beam was calculated by measuring the height of the beam and the transverse position at a given point between the HC mirrors as displayed in **Figure 29**. This was done close to the gold mirror and close to the silver mirror on the opposite side. From the distance between the points, it was possible to determine the input angle of the beam, which was calculated to have an x-angle [0.009

± 0.006] rad and a y-angle of [0.011 ± 0.006] rad.

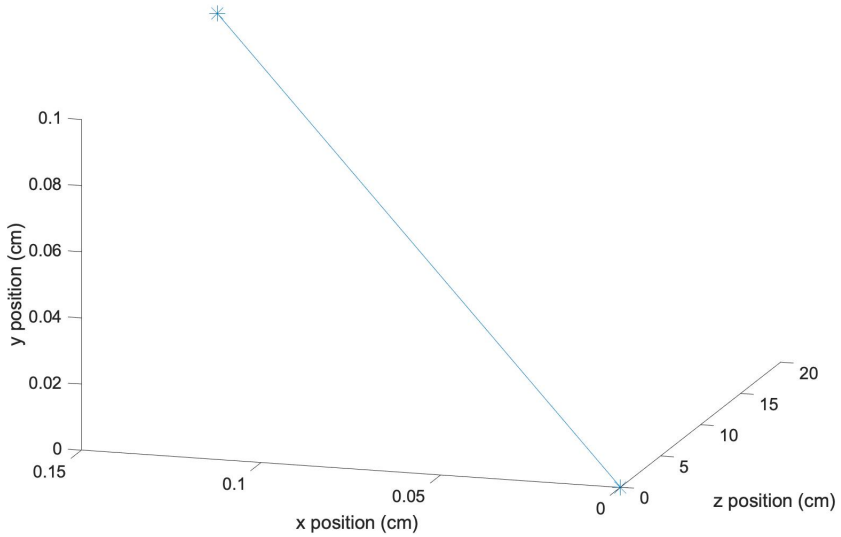

Figure 29: The position in the xy plane is measured at two different points separated by 17 cm in the z plane, i.e., moving from the entrance hole towards the opposite mirror

Comparing our results to the theoretical simulations found that with the exception of the spikes in the data, the red zone of **Figure 28a** matches with the curve in **Figure 28b** within the uncertainty of the length measurements. The spikes indicate that with precise positioning of the mirrors, alignment would potentially be possible. However, practically, it is difficult to achieve the plateaus with a smaller range of acceptable cell lengths. Perhaps this is why the smaller plateau that appears in **Figure 28a** at 35.6 cm length is not present in **Figure 28b** and only the next plateau is present.

3.6.3 Mode Fidelities

Recall that we are interested in using the HC for image preservation. Any image can be decomposed into a basis of HG modes, so if the HC can preserve these modes, it can preserve general images. The modes are analyzed to determine their fidelity, a measure of the mode quality with 100% fidelity being an ideal mode. The first step in calculating the fidelity of the HC is to reconstruct the modes as described in Section 3.5.3. **Figure 30** shows sample mode reconstructions for HG00 for both the HC and the flip mirror. Higher-order modes are included for reference in Appendix A. The flip mirror case is included to calculate the degradation caused by the HC itself rather than the other optical elements in the setup.

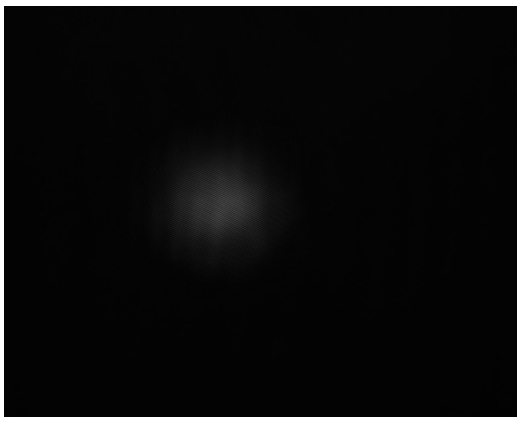

(a) HG00 mode as recorded by the camera after an HC with total delay of 7.9 m

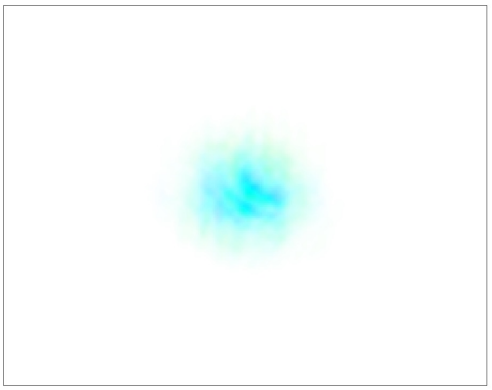

(b) Reconstructed HG00 mode from the HC

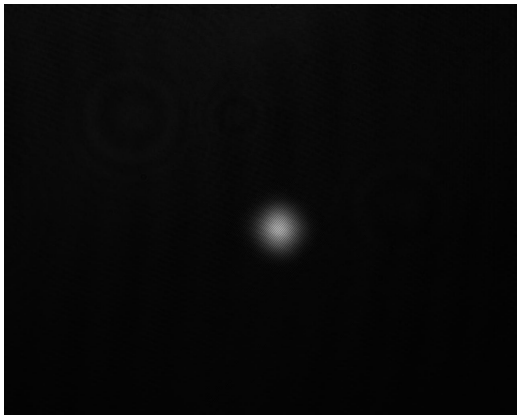

(c) HG00 mode as recorded by the camera after a the flip mirror, i.e., no HC, 0 m delay

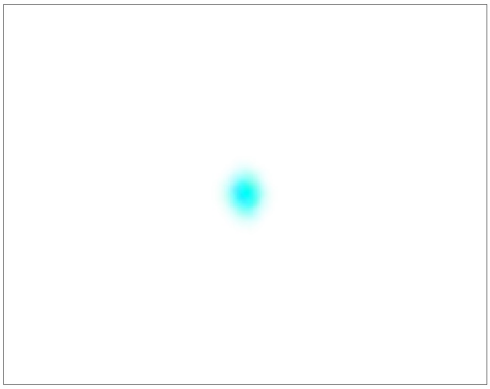

(d) Reconstructed HG00 mode from the flip mirror

Figure 30: Images recorded by the CCD camera and the subsequent mode reconstructions for HG00 using a HC with delay of 7.9 m or a flip mirror to bypass the HC and provide no delay.

The fidelity for both cases is calculated by comparing the reconstructed mode to an ideal mode. This ideal mode is chosen through an optimization process to determine the appropriate parameters (centre position of the beam, tilt phase, beam size, defocusing, beam rotation angle) for each iteration. The data collection process was automated except for the movement of the translation stage. Once the stage was set at a given plateau, the modes would cycle through HG00, HG10, HG01, HG11, HG20, HG02, HG21, HG12, HG30, HG03. This was then repeated 10 times. We found that the parameters throughout the many iterations were indeed quite consistent, although there was a bit of beam wandering as shown in **Figure 31**. This beam wandering was more noticeable for the HC than for the flip mirror. A potential cause for this discrepancy is that one of the mirrors in the HC is mounted on a translation stage which could be unstable. Despite this, the beam drift (20 μm) was still minimal compared to the size of the

beam diameter (600 μm) for the HC measurements.

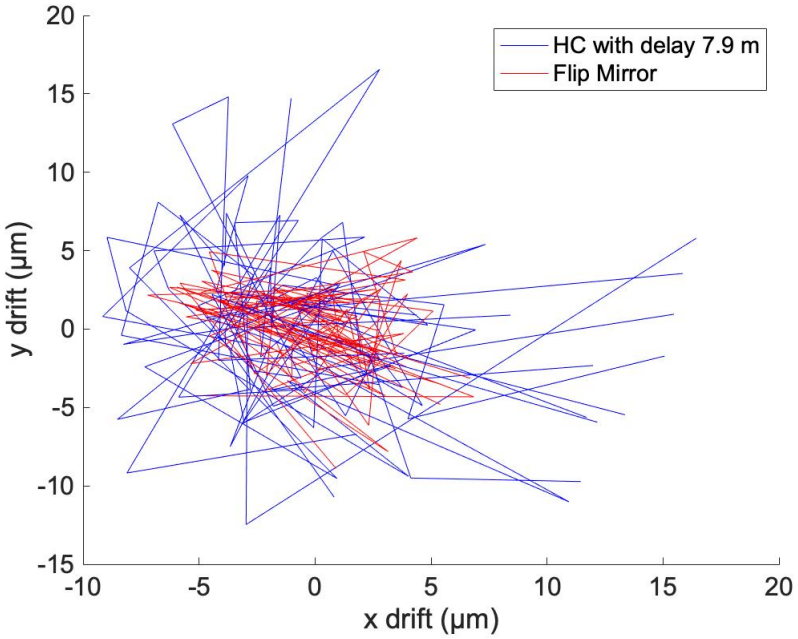

Figure 31: Illustration showing tracking of the centre of the beam through the hundred images recorded with the CCD camera for a delay of 7.9 m and with no delay. Although the beam wanders, it never ventures further than 20 μm from the centre.

The ideal parameters are then averaged to create a single set of parameters. This final set of parameters is then used to calculate the fidelity for all iterations without further optimizations. The ratio of the fidelities for the HC and the flip mirror is used to calculate the degradation due to the cell itself since both the flip mirror and the HC share the same path to the camera. For one iteration, the HC fidelity is divided by the flip mirror fidelity for that iteration. The mean of these values is then used to calculate the average fidelity. This average fidelity for each mode compared to the delay is plotted in **Figure 32**. The error bars are the standard deviation of the fidelities for different iterations.

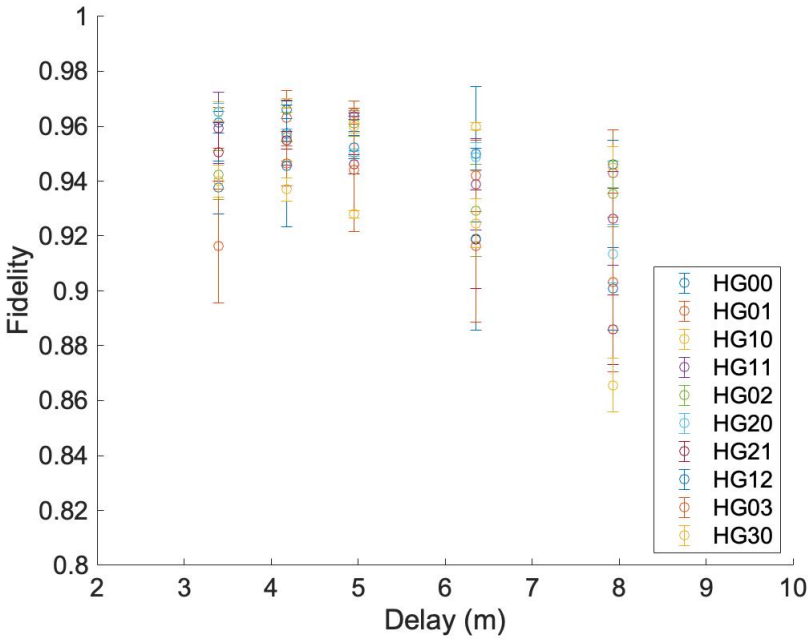

Figure 32: Average fidelity for each mode compared to the delay length of the HC

Note that fairly high fidelities (>90%) can be achieved for almost all modes with a low of 86%. There was a slight decrease in the fidelities as the delay was increased, which makes sense as the propagation is longer and there are more reflections from the mirrors. There also appears to be a slight decrease as the mode order increases, this is especially true at the larger delay lengths. Higher-order modes are larger giving them more chance to interact with imperfections or leak off the edge of the mirrors. However, it does not occur to a degree that would be deemed concerning, especially at the shorter delay lengths. This observation also raised the question of mirror quality required for our application. Most mirrors are designed to have a single reflection and are usually specified to a surface irregularity of $\lambda/4$, which would mean that for N round trips, a conservative estimate for the quality required would be $\lambda/4N$. However, it is unlikely that this is a limiting factor for our set up since high fidelities were observed with the quality of the mirrors employed in the experiment. However, this feature may merit further discussion and exploration in the future.

Our results with the HG modes are encouraging since they suggest that the preservation of images is possible. To assess this notion, we attempted to image different shapes through the HC, which will be described in Section 3.6.6.

3.6.4 Mode Efficiencies

In **Figure 33** the efficiency of each mode is compared to the delay. This comparison was computed by comparing the intensity of light after the HC to the intensity of light from the flip mirror, i.e., no HC.

Previously, our simulations suggested that 100% efficiencies should be achieved. However, this simply assumed that the mode would be wholly on the mirrors and did not account for the losses due to the efficiencies of the mirrors themselves. In this case, it makes sense that as the number of reflections increases and the delay increases, the efficiency decreases. However, this was not considered to be a limiting problem since it is possible to make dielectric mirrors with efficiencies $> 99.999\%$ [64]. For comparison, the mirrors in our experimental setup had efficiencies of 97-98%.

The theoretical efficiency is calculated by counting the number of reflections and then raising the efficiencies of the mirrors to this power. A lower and upper bound to the theoretical efficiency may be calculated based on the values quoted by Thorlabs for their mirror performances. Note the difference is on the order of 1% which after many reflections in the HC translates to a large change in the overall efficiencies.

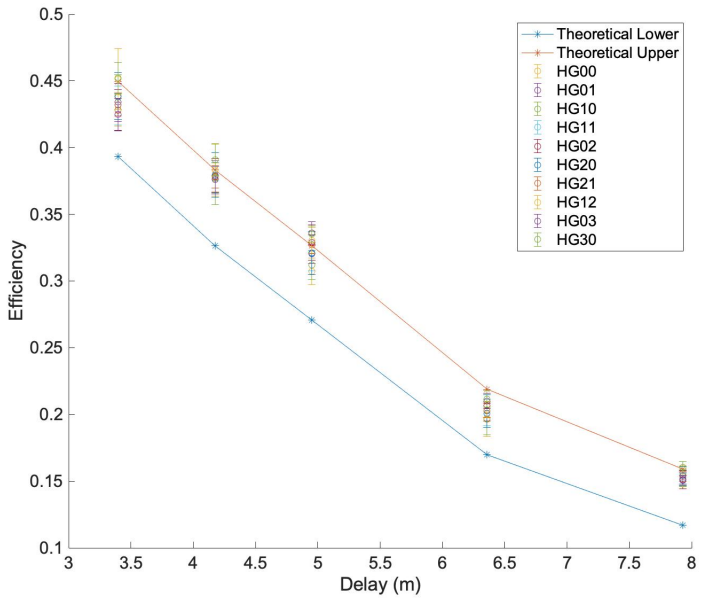

Figure 33: Average efficiency for each mode compared to the delay length of the HC

We may also note, the reflection numbers were counted using a red visible (650 nm) laser while the mode measurements were obtained using a 795 nm IR laser. This difference in wavelength affects the

output from the SLM, which means that the incoming angle to the HC will be different than if the visible laser is used. Our simulations revealed that the input angle controls the reflection numbers and consequently fewer reflections may be occuring than anticipated. This would also imply the delay is less than expected.

3.6.5 System Resolution

It is often desirable to know the resolution of imaging systems. In the present work, we demonstrate the ability of the HC to preserve an image with a given resolution as it passes through the cell. The Modulation Transfer Function (MTF) provides a measurement of a system's ability to preserve contrast (modulation) at a given resolution (measured as a grating in lines/mm) [67]. The MTF curve is calculated by imaging a series of bars with given thicknesses and therefore a certain frequency of lines/mm through the HC. Upon exiting, the image of originally fully contrasting bars are then measured and fitted to record the contrast. The result is shown in **Figure 34**. Traditionally the curve would be plotted as contrast with respect to lines/mm. However, it could be more intuitive to speak of resolution as a distance, e.g. what is the smallest separation we could resolve. So for our system, we inverted this lines/mm, plotting contrast with respect to the width of the lines at the HC. Lines are generated on the SLM (pixel size 9 μm) and imaged on to the HC hole using a 4f system which decreases the size of the image by a factor of 2.5. Thinking in terms of the line width as pixels on the SLM allows us to take into consideration the quality of image generation and the effects this may have on the contrast.

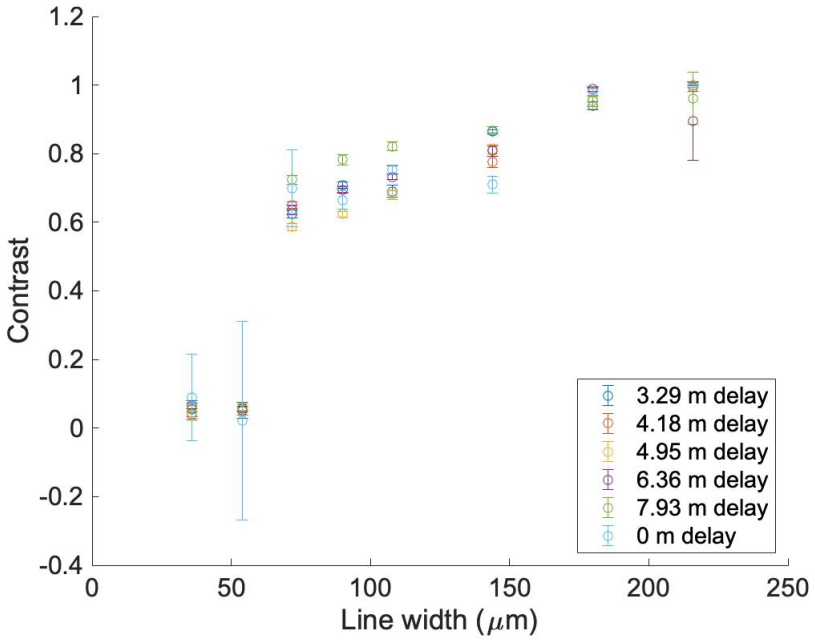

Figure 34: Modulation transfer function for an HC of varying delay lengths. This function is a measure of the ability of an imaging system to preserve contrast for a given resolution.

As with the mode images, we once again compare to a flip mirror to consider the degradation solely due to the cell. In this case, it is important to consider the limitations of the SLM. As the lines/mm increase (the width of the lines decreases) and the contrast drops to 0, it is in part due to the inability of the SLM to produce the image at this resolution. Perhaps, the SLM is not able to generate images with details smaller than 20 pixels (corresponding to 72 μm at the HC). We can see this by noting that the contrast with the flip mirror, or without delay, is roughly the same as that of the delayed HC. It is also interesting to note that at roughly 70 μm, the lines become resolvable. The contrast then increases until a linewidth of roughly 180 μm is reached where the lines become consistently created and preserved with the high contrast. We measured vertical lines, however for a full characterization of the resolution and aberrations in the system , these contrast measurements should be taken for lines in both the x and y directions.

3.6.6 Sample Images

Let us remember the original goal of this project is to show that the HC can be used as an image-preserving delay line (IPDL). As a demonstration of this application, **Figure 35** shows two images: 1. the letter A and 2. the University of Ottawa logo under the following conditions (a) original, (b) passed through the HC with a 7.9 m delay, and finally (c) bypassing the HC, 0 m delay from the flip mirror.

Clearly, the HC can preserve these images and could be used as an IPDL. More images can be found in Appendix B. As mentioned earlier, the field was digitally propagated to the image plane to view these images. Note that the image quality is dependent on the initial production from the SLM and on the reconstruction method which limits the available resolution.

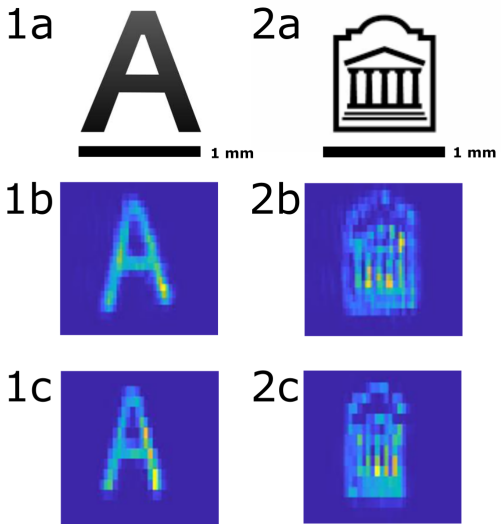

Figure 35: Images for the letter A (1) and the logo for the University of Ottawa (2) under three different conditions: (a) original images, (b) images passed through a 7.9 m delay in the HC, and (c) the image with a 0 m delay from the flip mirror

3.7 Proof of Concept Experiments and Future Work

3.7.1 Electronic Power Limiter

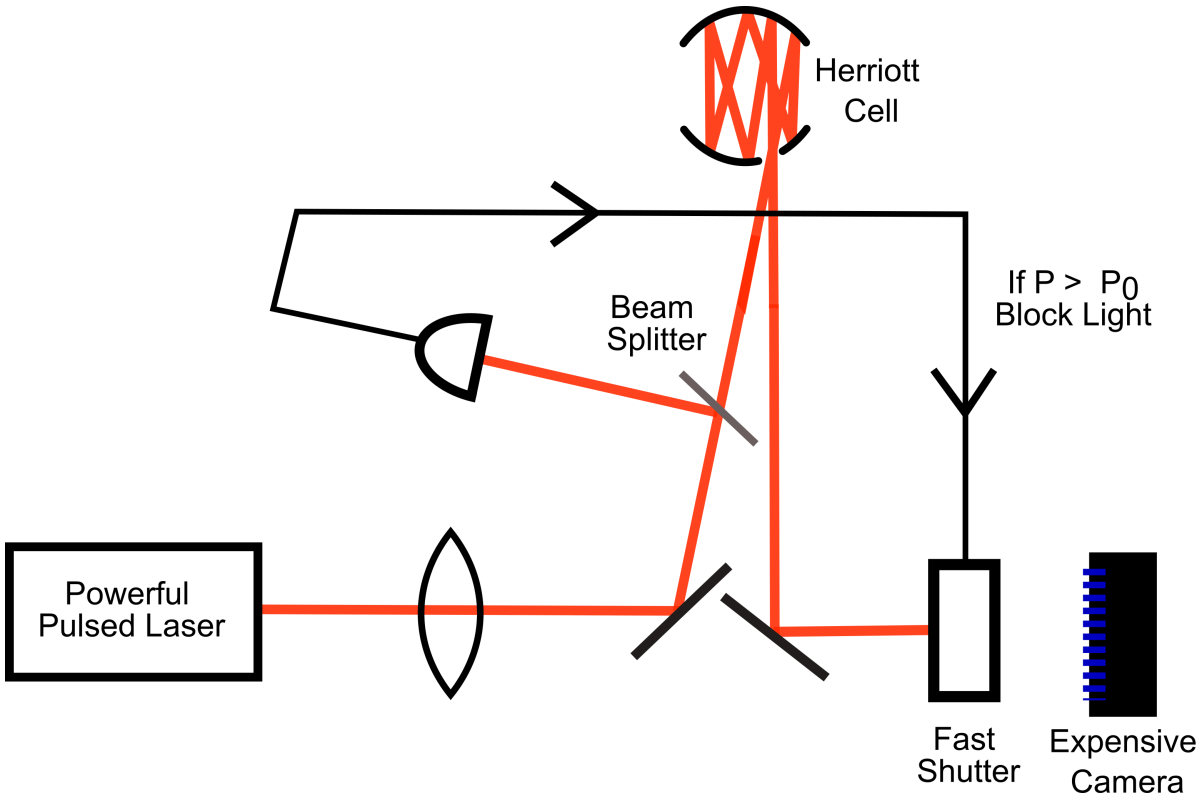

Figure 36: Using the HC as a delay component in an electronic power limiter to protect against bright illumination attacks

Currently, we are in the process of designing an electronic power limiter using the HC. Optical power limiters are used to secure quantum cryptosystems against bright illumination attacks [68]. The concept is shown in **Figure 36** and functions as follows. Consider imaging an arbitrary scene, located in the same position as the powerful pulsed laser. The imaging system is set up so that the beam passes through the HC before reaching the camera. The beam is sampled in a known percentage so that the power can be measured. Then if a bright light source (i.e., power above a certain predetermined threshold, $P > P_0$) were to shine while the beam is delayed in the HC, we could operate a shutter to block the beam and protect the camera.

3.8 Conclusion

In conclusion, we demonstrated the use of a Herriott cell as an image-preserving delay line. It preserved general images suitably when examined by eye. Many delay lengths were reached from 3.4 m to 7.9 m

with only minor adjustments (<3 cm using a translation stage) to the cell length. To generalize the idea of image preservation, we tested HG modes as they form an orthogonal basis, i.e. any image can be decomposed into a sum of these modes. We tested 10 of the lower-order HG modes and they were found to be preserved with a fidelity of >90% for almost all of these delays. The exceptions being the largest modes (HG03 and HG30) at the longest delay of 7.9 m where fidelity was >86%. Overall, the simplicity of the Herriott cell and ease of alignment make it a good image-preserving delay line. It would be especially useful in applications where space is valuable, e.g., miniaturization. The future work planned for this experiment would be to build an electronic power limiter (detailed in Section 3.7) as a proof of concept.

4 General Conclusion

Overall, this thesis has presented two separate projects which offer new insight into the world of quantum imaging. In Chapter 2, with the goal of increasing imaging resolution and breaking "Rayleigh's Curse", we generalized the standard Richardson-Lucy deconvolution algorithm and applied it to a Zernike mode sorter-based confocal microscope in order to achieve super-resolution. We tested our approach and found it was able to resolve general scenes with arbitrary geometry. In comparison with the conventional confocal microscopy using the standard RL algorithm, the resolution enhancement for the sorter-based microscopy using the generalized RL algorithm was over 30% higher. This method is simple as it uses linear light and does not require additional manipulation of the sample. Consequently, this method affords a good option to be used in combination with existing super-resolution methods for further resolution enhancement.

In Chapter 3, we demonstrated the use of a Herriott cell as an image-preserving delay line. IPDLs, which are traditionally a series of 4f systems, are commonly employed in quantum imaging experiments requiring delay time to account for the latency of many detection systems. The HC was able to achieve controllable delay lengths, ranging from 3.4 m to 7.9 m with only minor adjustments (<3 cm using a translation stage) to the cell length and no additional realignment. The preservation of 10 of the lower-order HG modes was tested and it was found that the they were preserved with a fidelity of >90% for almost all of these delays, with exceptions being the largest modes (HG03 and HG30) at the longest delay (7.9 m) where the fidelity was still >86%. HG modes were chosen as they form an orthogonal basis, i.e., any image can be decomposed into a sum of these modes. The compact nature and ease of alignment of the HC make it a good IPDL and especially useful in applications where space is valuable.

A Mode Reconstructions

The following measurements were taken at 5 different plateaus with varying delay distances from 3.4 m to 7.9 m, as well as a flip mirror to provide the case with no delay. As an example, the 7.9-m delay is shown for the first 10 HG modes (**Figure 37**). Appendix B displays images through the same 7.9-m delay.

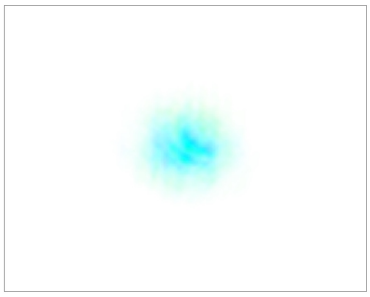

(a) HG00

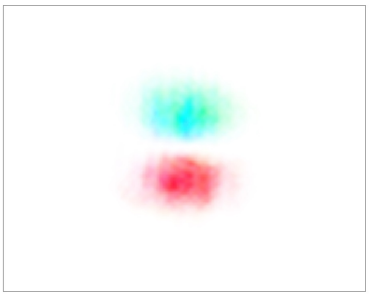

(b) HG01

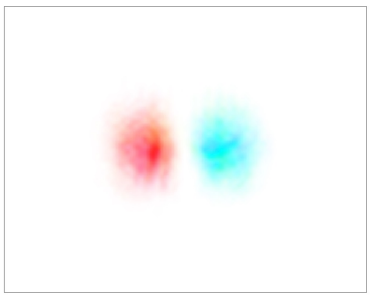

(c) HG10

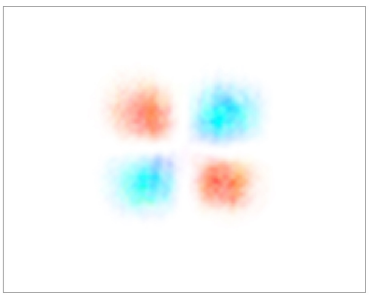

(d) HG11

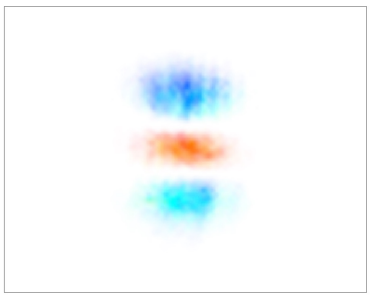

(e) HG02

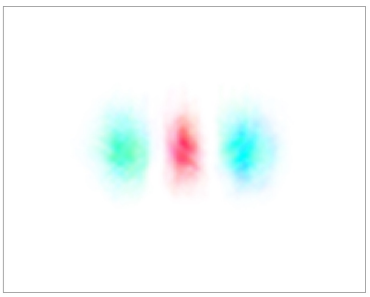

(f) HG20

(g) HG12

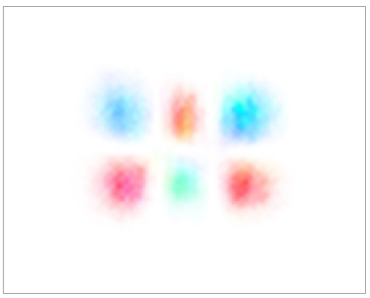

(h) HG21

(i) HG03

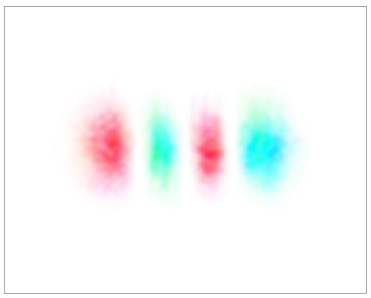

(j) HG30

Figure 37: Reconstructed HG modes (570 μm beam waist) for a 7.9-m Herriott cell delay

B Additional Images

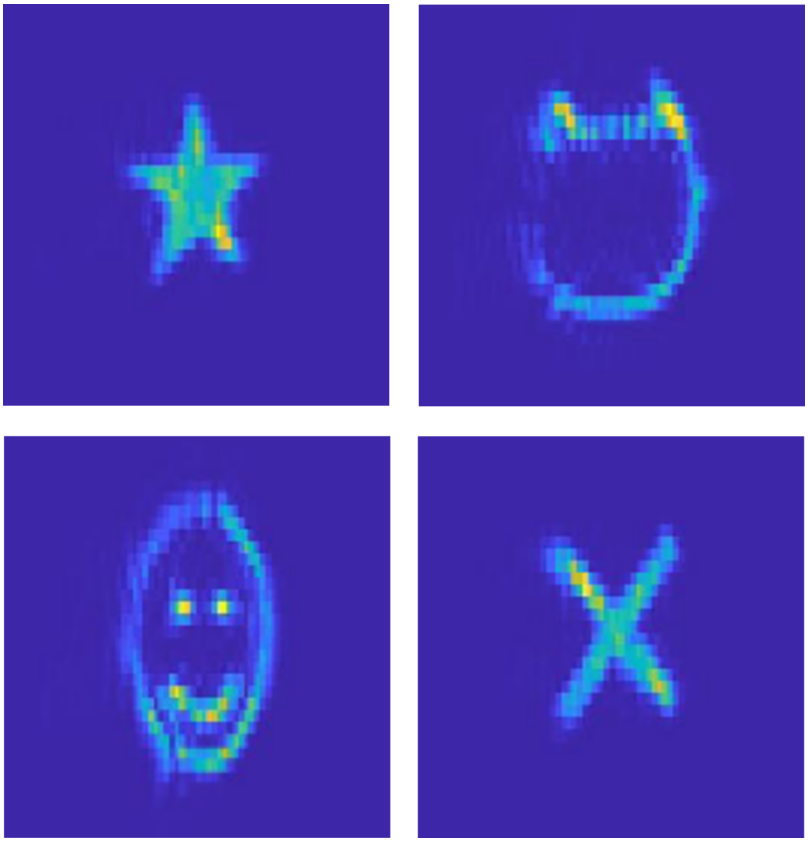

Figure 38: Additional images (width of 1 mm) that have been delayed for 7.9 m through a Herriott cell

C Copyright Permissions

THE AMERICAN ASSOCIATION FOR THE ADVANCEMENT OF SCIENCE LICENSE TERMS AND CONDITIONS

May 16, 2022

This Agreement between Katherine Bearne ("You") and The American Association for the Advancement of Science ("The American Association for the Advancement of Science") consists of your license details and the terms and conditions provided by The American Association for the Advancement of Science and Copyright Clearance Center.

License Number	5305520989829
License date	May 10, 2022
Licensed Content Publisher	The American Association for the Advancement of Science
Licensed Content Publication	Science
Licensed Content Title	Imaging Intracellular Fluorescent Proteins at Nanometer Resolution
Licensed Content Author	Eric Betzig, George H. Patterson, Rachid Sougrat, O. Wolf Lindwasser, et al.
Licensed Content Date	Sep 15, 2006
Licensed Content Volume	313
Licensed Content Issue	5793
Volume number	313
Issue number	5793
Type of Use	Thesis / Dissertation
Requestor type	Scientist/individual at a research institution
Format	Electronic
Portion	Text Excerpt
Number of pages requested	1
Title	Novel Techniques in Quantum Optics
Institution name	University of Ottawa
Expected presentation date	May 2022
Portions	Figure 2.
Requestor Location	Katherine Bearne 25 Templeton St Ottawa, ON K1N 6N5 Canada Attn: University of Ottawa
Total	**0.00 CAD**

Terms and Conditions

American Association for the Advancement of Science TERMS AND CONDITIONS

Regarding your request, we are pleased to grant you non-exclusive, non-transferable permission, to republish the AAAS material identified above in your work identified above, subject to the terms and conditions herein. We must be contacted for permission for any uses other than those specifically identified in your request above.
The following credit line must be printed along with the AAAS material: "From [Full Reference Citation]. Reprinted with permission from AAAS."
All required credit lines and notices must be visible any time a user accesses any part of the AAAS material and must appear on any printed copies and authorized user might make.
This permission does not apply to figures / photos / artwork or any other content or materials included in your work that are credited to non-AAAS sources. If the requested material is sourced to or references non-AAAS sources, you must obtain authorization from that source as well before using that material. You agree to hold harmless and indemnify AAAS against any claims arising from your use of any content in your work that is credited to non-AAAS sources.
If the AAAS material covered by this permission was published in Science during the years 1974 - 1994, you must also obtain permission from the author, who may grant or withhold permission, and who may or may not charge a fee if permission is granted. See original article for author's address. This condition does not apply to news articles.
The AAAS material may not be modified or altered except that figures and tables may be modified with permission from the author. Author permission for any such changes must be secured prior to your use.
Whenever possible, we ask that electronic uses of the AAAS material permitted herein include a hyperlink to the original work on AAAS's website (hyperlink may be embedded in the reference citation).
AAAS material reproduced in your work identified herein must not account for more than 30% of the total contents of that work.
AAAS must publish the full paper prior to use of any text.
AAAS material must not imply any endorsement by the American Association for the Advancement of Science.
This permission is not valid for the use of the AAAS and/or Science logos.
AAAS makes no representations or warranties as to the accuracy of any information contained in the AAAS material covered by this permission, including any warranties of
merchantability or fitness for a particular purpose.
If permission fees for this use are waived, please note that AAAS reserves the right to charge for reproduction of this material in the future.
Permission is not valid unless payment is received within sixty (60) days of the issuance of this permission. If payment is not received within this time period then all rights granted herein shall be revoked and this permission will be considered null and void.
In the event of breach of any of the terms and conditions herein or any of CCC's Billing and Payment terms and conditions, all rights granted herein shall be revoked and this permission will be considered null and void.
AAAS reserves the right to terminate this permission and all rights granted herein at its discretion, for any purpose, at any time. In the event that AAAS elects to terminate this permission, you will have no further right to publish, publicly perform, publicly display, distribute or otherwise use any matter in which the AAAS content had been included, and all fees paid hereunder shall be fully refunded to you. Notification of termination will be sent to the contact information as supplied by you during the request process and termination shall be immediate upon sending the notice. Neither AAAS nor CCC shall be liable for any costs, expenses, or damages you may incur as a result of the termination of this permission, beyond the refund noted above.
This Permission may not be amended except by written document signed by both parties.
The terms above are applicable to all permissions granted for the use of AAAS material. Below you will find additional conditions that apply to your particular type of use.

FOR A THESIS OR DISSERTATION

If you are using figure(s)/table(s), permission is granted for use in print and electronic versions of your dissertation or thesis. A full text article may be used in print versions only of a dissertation or thesis.
Permission covers the distribution of your dissertation or thesis on demand by ProQuest / UMI, provided the AAAS material covered by this permission remains in situ.
If you are an Original Author on the AAAS article being reproduced, please refer to your License to Publish for rules on reproducing your paper in a dissertation or thesis.

FOR JOURNALS:

Permission covers both print and electronic versions of your journal article, however the AAAS material may not be used in any manner other than within the context of your article.

FOR BOOKS/TEXTBOOKS:

If this license is to reuse figures/tables, then permission is granted for non-exclusive world rights in all languages in both print and

RE: Copyright Permission Request

Optica Publishing Group Copyright <copyright@osa.org>
Tue 2022-05-17 1:47 PM

To: Katherine Bearne <[redacted]>;Optica Publishing Group Copyright <copyright@osa.org>

Dear Dr. Bearne,

Thank you for contacting Optica Publishing Group.

For the use of figures 11 and 18 from Donald R. Herriott and Harry J. Schulte, "Folded Optical Delay Lines," Appl. Opt. 4, 883-889 (1965):

> Optica Publishing Group considers your requested use of its copyrighted material to be Fair Use under United States Copyright Law. We request that a complete citation of the original material be included in any publication.

For the use of figure 2 from Manuel Unternährer, Bänz Bessire, Leonardo Gasparini, Matteo Perenzoni, and André Stefanov, "Super-resolution quantum imaging at the Heisenberg limit," Optica 5, 1150-1154 (2018):

> Optica Publishing Group considers your requested use of its copyrighted material to be Fair Use under United States Copyright Law. We request that a complete citation of the original material be included in any publication.
>
> As this article is published under the terms of the Optica Publishing Group Open Access Publishing Agreement, when adapting or otherwise creating a derivative version of the article, users must maintain attribution to the author(s) and the published article's title, journal citation, and DOI. Users should also indicate if changes were made and avoid any implication that the author or Optica Publishing Group endorses the use.

While your publisher should be able to provide additional guidance, we prefer the below citation formats:

> For citations in figure captions:
>
> [Reprinted/Adapted] with permission from [ref #] © The Optical Society. (Please include the full citation in your reference list)
>
> For images without captions:
>
> Journal Vol. #, first page (year published) An example: Biomed. Opt. Express 6, 793 (2015)

Please let me know if you have any questions.

Kind Regards,
Hannah Greenwood

Hannah Greenwood
May 17, 2022
Authorized Agent, Optica Publishing Group

OPTICA PUBLISHING GROUP | Formerly OSA

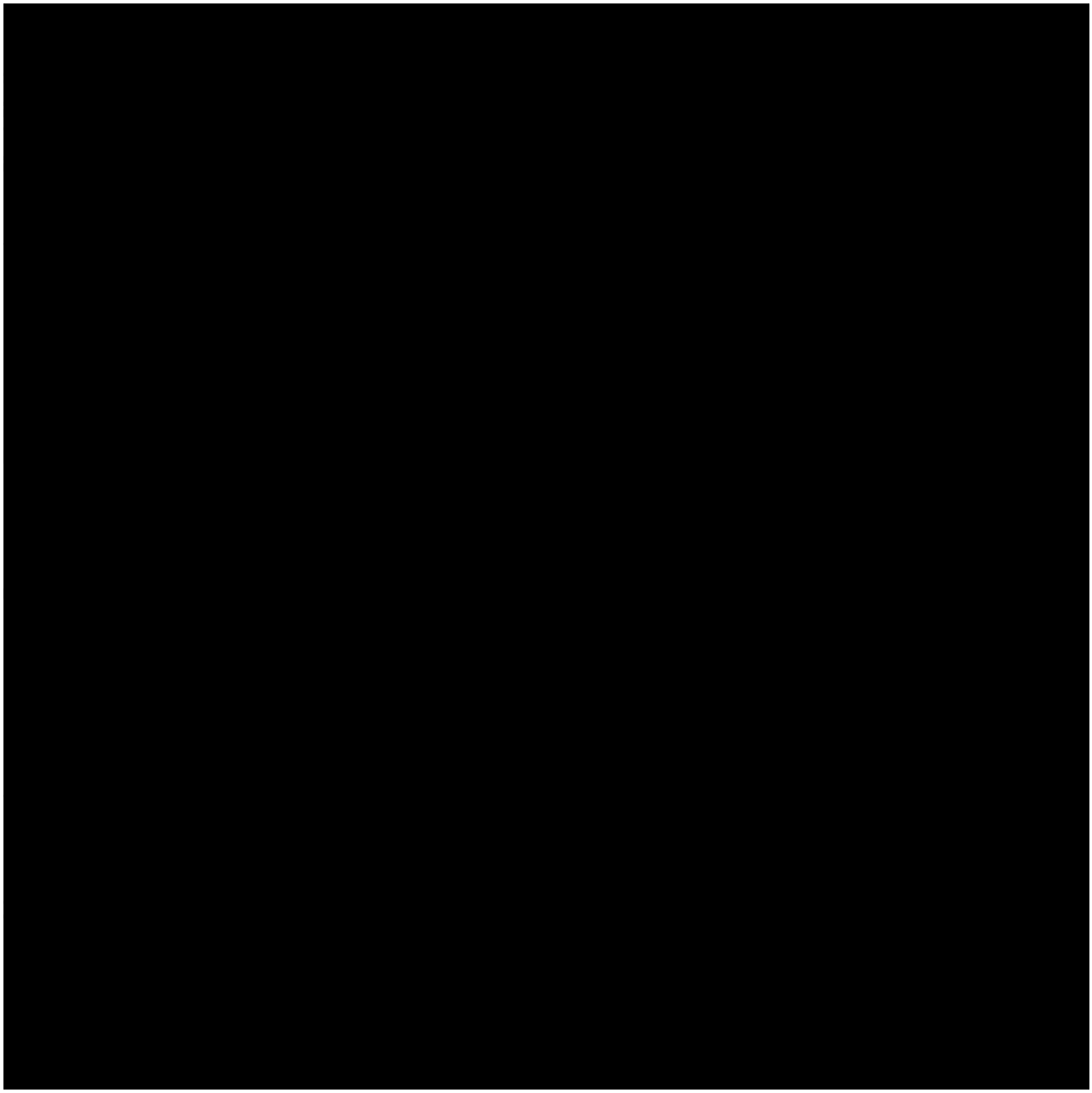

RE: Copyright Permission Request

Optica Publishing Group Copyright <copyright@osa.org>

Thu 2021-12-02 1:38 PM

To: Katherine Bearne [redacted];Optica Publishing Group Copyright <copyright@osa.org>

Dear Katherine Bearne,

Thank you for contacting Optica Publishing Group.
For the use of material from Katherine K. M. Bearne, Yiyu Zhou, Boris Braverman, Jing Yang, S. A. Wadood, Andrew N. Jordan, A. N. Vamivakas, Zhimin Shi, and Robert W. Boyd, "Confocal super-resolution microscopy based on a spatial mode sorter," Opt. Express 29, 11784-11792 (2021):

> Because you are the author of the source paper from which you wish to reproduce material, Optica Publishing Group considers your requested use of its copyrighted materials to be permissible within the author rights granted in the Copyright Transfer and Open Access Publishing Agreement submitted by the requester on acceptance for publication of his/her manuscript. It is requested that a complete citation of the original material be included in any publication. This permission assumes that the material was not reproduced from another source when published in the original publication.
>
> If the entire article is being included, it is permissible to use the **version of record**.

While your publisher should be able to provide additional guidance, we prefer the below citation formats:

> For citations in figure captions:
>
> [Reprinted/Adapted] with permission from [ref #] © Optica Publishing Group. (Please include the full citation in your reference list)
>
> For images without captions:
>
> Journal Vol. #, first page (year published) An example: Opt. Express 19, 2720 (2011)

Please let me know if you have any questions.

Kind Regards,
Hannah Greenwood

Hannah Greenwood
December 2, 2021
Authorized Agent, Optica Publishing Group

OPTICA PUBLISHING GROUP | Formerly OSA

References

[1] Lord Rayleigh. XXXI. Investigations in optics, with special reference to the spectroscope. *Philos. Mag. Ser.*, 8(49):261–274, 1879.

[2] E. Abbe. Beiträge zur theorie des mikroskops und der mikroskopischen wahrnehmung. *Archiv f. mikrosk. Anatomie*, 9:413–468, 1873.

[3] K. K. M. Bearne, Y. Zhou, B. Braverman, J. Yang, S. A. Wadood, A. N. Jordan, Vamivakas, A. N., Z. Shi, and R. W. Boyd. Confocal super-resolution microscopy based on a spatial mode sorter. *Optics Express*, 29:11784–11792, 2021.

[4] Walker J. G. Brinicombe A. M. Fish, D. A. and E. R. Pike. Confocal microscopy: comparisons, applications, and problems. *BioTechniques*, 39(6 supp), 2005.

[5] S. Hell and E. H. K. Stelzer. Properties of a 4pi confocal fluorescence microscope. *J. Opt. Soc. Am. A*, 19(12):2159, 1992.

[6] M. G. Gustafsson. Surpassing the lateral resolution limit by a factor of two using structured illumination microscopy. *J. Microsc.*, 198:82–87, 2000.

[7] Timothy R. Corle and Gordon S. Kino. Chapter 1 - introduction. In Timothy R. Corle and Gordon S. Kino, editors, *Confocal Scanning Optical Microscopy and Related Imaging Systems*, pages 1–66. Academic Press, Burlington, 1996.

[8] A. Marian, F. Charrière, T. Colomb, F. Montfort, J. Kühn, P. Marquet, and C. Depeursinge. On the complex three-dimensional amplitude point spread function of lenses and microscope objectives: theoretical aspects, simulations and measurements by digital holography. *J. Microsc.*, 225:156–169, 2007.

[9] George Biddell Airy. On the diffraction of an object-glass with circular aperture. *Trans. of the Cambridge Philosoph. Soc.*, 5:283–291, 1835.

[10] M. M. Abramowitz and I.A. Stegun. *Handbook of Mathematical Functions with Formulas, Graphs, and Mathematical Tables*. US Government printing office, 1972.

[11] Stefan W Hell and Jan Wichmann. Breaking the diffraction resolution limit by stimulated emission: stimulated-emission-depletion fluorescence microscopy. *Opt. Lett.*, 19(11):780–782, 1994.

[12] Eric Betzig, George H Patterson, Rachid Sougrat, O Wolf Lindwasser, Scott Olenych, Juan S Bonifacino, Michael W Davidson, Jennifer Lippincott-Schwartz, and Harald F Hess. Imaging intracellular fluorescent proteins at nanometer resolution. *Science*, 313(5793):1642–1645, 2006.

[13] Michael J Rust, Mark Bates, and Xiaowei Zhuang. Sub-diffraction-limit imaging by stochastic optical reconstruction microscopy (STORM). *Nat. Methods*, 3(10):793–796, 2006.

[14] Mankei Tsang. Quantum imaging beyond the diffraction limit by optical centroid measurements. *Phys. Rev. Lett.*, 102(25):253601, 2009.

[15] Heedeuk Shin, Kam Wai Clifford Chan, Hye Jeong Chang, and Robert W Boyd. Quantum spatial superresolution by optical centroid measurements. *Phys. Rev. Lett.*, 107(8):083603, 2011.

[16] Lee A Rozema, James D Bateman, Dylan H Mahler, Ryo Okamoto, Amir Feizpour, Alex Hayat, and Aephraim M Steinberg. Scalable spatial superresolution using entangled photons. *Phys. Rev. Lett.*, 112(22):223602, 2014.

[17] Manuel Unternährer, Bänz Bessire, Leonardo Gasparini, Matteo Perenzoni, and André Stefanov. Super-resolution quantum imaging at the Heisenberg limit. *Optica*, 5(9):1150–1154, 2018.

[18] Ermes Toninelli, Paul-Antoine Moreau, Thomas Gregory, Adam Mihalyi, Matthew Edgar, Neal Radwell, and Miles Padgett. Resolution-enhanced quantum imaging by centroid estimation of biphotons. *Optica*, 6(3):347–353, 2019.

[19] Ron Tenne, Uri Rossman, Batel Rephael, Yonatan Israel, Alexander Krupinski-Ptaszek, Radek Lapkiewicz, Yaron Silberberg, and Dan Oron. Super-resolution enhancement by quantum image scanning microscopy. *Nat. Photon.*, 13(2):116–122, 2019.

[20] Osip Schwartz, Jonathan M Levitt, Ron Tenne, Stella Itzhakov, Zvicka Deutsch, and Dan Oron. Superresolution microscopy with quantum emitters. *Nano Lett.*, 13(12):5832–5836, 2013.

[21] Bessire B. Gasparini L. Perenzoni M. Unternährer, M. and A. Stefanov. Super-resolution quantum imaging at the heisenberg limit. *Optica*, 5:1150–1154, 2018.

[22] Mankei Tsang, Ranjith Nair, and Xiao-Ming Lu. Quantum theory of superresolution for two incoherent optical point sources. *Phys. Rev. X*, 6(3):031033, 2016.

[23] Fan Yang, Arina Tashchilina, Eugene S Moiseev, Christoph Simon, and Alexander I Lvovsky. Far-field linear optical superresolution via heterodyne detection in a higher-order local oscillator mode. *Optica*, 3(10):1148–1152, 2016.

[24] Martin Paúr, Bohumil Stoklasa, Zdenek Hradil, Luis L Sánchez-Soto, and Jaroslav Rehacek. Achieving the ultimate optical resolution. *Optica*, 3(10):1144–1147, 2016.

[25] Weng-Kian Tham, Hugo Ferretti, and Aephraim M Steinberg. Beating Rayleigh's curse by imaging using phase information. *Phys. Rev. Lett.*, 118(7):070801, 2017.

[26] Zong Sheng Tang, Kadir Durak, and Alexander Ling. Fault-tolerant and finite-error localization for point emitters within the diffraction limit. *Opt. Express*, 24(19):22004–22012, 2016.

[27] Yiyu Zhou, Jing Yang, Jeremy D Hassett, Seyed Mohammad Hashemi Rafsanjani, Mohammad Mirhosseini, A Nick Vamivakas, Andrew N Jordan, Zhimin Shi, and Robert W Boyd. Quantum-limited estimation of the axial separation of two incoherent point sources. *Optica*, 6(5):534–541, 2019.

[28] Francesco Albarelli, Jamie F Friel, and Animesh Datta. Evaluating the Holevo Cramér-Rao bound for multiparameter quantum metrology. *Phys. Rev. Lett.*, 123(20):200503, 2019.

[29] Mankei Tsang. Semiparametric estimation for incoherent optical imaging. *Phys. Rev. Research*, 1(3):033006, 2019.

[30] Sisi Zhou and Liang Jiang. Modern description of Rayleigh's criterion. *Phys. Rev. A*, 99(1):013808, 2019.

[31] Jing Yang, Shengshi Pang, Yiyu Zhou, and Andrew N Jordan. Optimal measurements for quantum multiparameter estimation with general states. *Phys. Rev. A*, 100(3):032104, 2019.

[32] Mankei Tsang. Subdiffraction incoherent optical imaging via spatial-mode demultiplexing. *New J. Phys.*, 19(2):023054, 2017.

[33] J Řehaček, Z Hradil, B Stoklasa, M Paúr, J Grover, A Krzic, and LL Sánchez-Soto. Multiparameter quantum metrology of incoherent point sources: towards realistic superresolution. *Phys. Rev. A*, 96(6):062107, 2017.

[34] Xiao-Ming Lu, Hari Krovi, Ranjith Nair, Saikat Guha, and Jeffrey H Shapiro. Quantum-optimal detection of one-versus-two incoherent optical sources with arbitrary separation. *npj Quantum Inf.*, 4(1):1–8, 2018.

[35] Sudhakar Prasad. Quantum limited source localization and pair superresolution in two dimensions under finite-emission bandwidth. *Phys. Rev. A*, 102(3):033726, 2020.

[36] Kent AG Bonsma-Fisher, Weng-Kian Tham, Hugo Ferretti, and Aephraim M Steinberg. Realistic sub-Rayleigh imaging with phase-sensitive measurements. *New J. Phys.*, 21(9):093010, 2019.

[37] Mankei Tsang. Efficient superoscillation measurement for incoherent optical imaging. *arXiv:2010.11084*, 2020.

[38] Lijun Peng and Xiao-Ming Lu. Generalization of Rayleigh's curse on parameter estimation with incoherent sources. *arXiv:2011.07897*, 2020.

[39] William Hadley Richardson. Bayesian-based iterative method of image restoration. *J. Opt. Soc. Am.*, 62(1):55–59, 1972.

[40] Leon B Lucy. An iterative technique for the rectification of observed distributions. *Astron. J.*, 79:745, 1974.

[41] Blanc-Feraud L. Zimmer C. Roux P. Kam Z. Olivo-Marin J. C. Dey, N. and J Zerubia. Richardson-lucy algorithm with total variation regularization for 3d confocal microscope deconvolution. *Microsc. Res. Techniq.*, 69(4):260–266, 2006.

[42] Van Vliet L. J. Verveer P. J. Van Kempen, G. M. P. and H. T. M. Van Der Voort. A quantitative comparison of image restoration methods for confocal microscopy. *J. Microsc.*, 185(3):354–365, 1997.

[43] Walker J. G. Brinicombe A. M. Fish, D. A. and E. R. Pike. Blind deconvolution by means of the richardson–lucy algorithm. *J. Opt. Soc. Am. A*, 12(1):58, 1995.

[44] Zhixian Yu and Sudhakar Prasad. Quantum limited superresolution of an incoherent source pair in three dimensions. *Phys. Rev. Lett.*, 121(18):180504, 2018.

[45] Kamal Nasrollahi and Thomas B Moeslund. Super-resolution: a comprehensive survey. *Mach. Vision Appl.*, 25(6):1423–1468, 2014.

[46] TJ Herbert. Statistical stopping criteria for iterative maximum likelihood reconstruction of emission images. *Phys. Med. Biol.*, 35(9):1221, 1990.

[47] Yann LeCun, Léon Bottou, Yoshua Bengio, and Patrick Haffner. Gradient-based learning applied to document recognition. *Proc. of the IEEE*, 86(11):2278–2324, 1998.

[48] P. Kwiat, H. Weinfurter, T. Herzog, A. Zeilinger, and M. A. Kasevich. Interaction-free measurement. *Phys. Rev. Lett.*, 74(24):4763–4766, 1995.

[49] A. G. White, J. R. Mitchell, O. Nairz, and P. G. Kwiat. Interaction-free" imaging. *Phys. Rev. A*, 58(1):605–613, 1998.

[50] A. C. Elitzur and L. Vaidman. Quantum mechanical interaction-free measurements. *Found. of Phys.*, 23(7):987–997, 1993.

[51] H. Kwiat, P.and Weinfurter and A. Zeilinger. Quantum seeing in the dark. *Sci. Am.*, 275(5):72–78, 1996.

[52] M. J. Padgett and R. W. Boyd. An introduction to ghost imaging: Quantum and classical. *Philos. Trans. R. Soc.*, 2017.

[53] E. Gatti, A.and Brambilla, M. Bache, and L. A. Lugiato. Ghost imaging with thermal light: Comparing entanglement and classical correlation. *Phys. Rev. Lett.*, 93(9), 2004.

[54] T. B. Pittman, Y. H. Shih, D. V. Strekalov, and A. V. Sergienko. Optical imaging by means of two-photon quantum entanglement. *Phys. Rev. A*, 52(5), 5.

[55] J. H. Shapiro and R. W. Boyd. The physics of ghost imaging. *Quantum Inf. Process.*, 11(4):949–993, 2012.

[56] G. B. Lemos, V. Borish, G. D. Cole, S. Ramelow, R. Lapkiewicz, and A. Zeilinger. Quantum imaging with undetected photons. *Nature*, 512(7515):409–412, 2014.

[57] Y. Zhang, A. Sit, F. Bouchard, H. Larocque, F. Grenapin, E. Cohen, A.C. Elitzur, J. L. Harden, R. W. Boyd, and E. Karimi. Interaction-free ghost-imaging of structured objects. *Opt. Express*, 27(3), 2019.

[58] D. R. Herriott. Spherical-mirror oscillating interferometer. *Appl. Opt.*, 2(8):865, 1963.

[59] D. Herriott, H. Kogelnik, and R. Kompfner. Off-axis paths in spherical mirror interferometers. *Appl. Opt.*, 3(4):523, 1964.

[60] D. R. Herriott and H. J. Schulte. Folded optical delay lines. *Appl. Opt.*, 4(8):883, 1965.

[61] C. G. Tarsitano and C. R. Webster. Multilaser herriott cell for planetary tunable laser spectrometers. *Appl. Opt.*, 46(28):6923–6935, 2007.

[62] Eugene Hecht. *Optics*. Addison-Wesley, Boston, MA, USA, 4^{th} edition, 2002.

[63] Daniel A. Steck. Classical and modern optics. http://steck.us/teaching, 2017.

[64] G. Rempe, R. Lalezari, R. J. Thompson, and H. J. Kimble. Measurement of ultralow losses in an optical interferometer. *Opt. Lett.*, 17(5):363, 1992.

[65] C. URosales-Guzmán and A. Forbes. *How to Shape Light with Spatial Light Modulators*. SPIE PRESS, 2017.

[66] Andri M. Gretarsson. Basic paraxial optics toolkit, , matlab central file exchange. https://www.mathworks.com/matlabcentral/fileexchange/15459-basic-paraxial-optics-toolkit, 2019. Online; accessed 20 Dec 2019.

[67] Warren J. Smith. *Modern Optical Engineering.* McGraw-Hill, Montreal, QC, CAN, 3^{rd} edition, 2000.

[68] G. Zhang, I. W. Primaatmaja, J. Y. Haw, X. Gong, C. Wang, and C. C. W. Lim. Securing practical quantum cryptosystems with optical power limiters. *PRX Quantum*, 2(3), 2021.